Nano Research

Open Access

Research Article

Small extracellular vesicles loaded with neurotrophin-3 confer multitargeted therapeutic effects in treating spinal cord injury

Fuxiang Li[1,§], Zhonghai Huang[1,§], Jinrui Zhou[2,§], Zicong Wu[3,4], Xiao-Hui Deng[3,4], Huandi Weng[1], Wanxing Peng[6], Jing Li[1,6], Ye Lin[1], Kwok-Fai So[1,7,8,9], Qing-Ling Fu[3,4,5] ✉, and Libing Zhou[1,7,8,9] ✉

[1] *State Key Laboratory of Bioactive Molecules and Druggability Assessment, Key Laboratory of CNS Regeneration-Ministry of Education, Guangdong Basic Research Center of Excellence for Natural Bioactive Molecules and Discovery of Innovative Drugs, Guangdong-Hongkong-Macau Institute of CNS Regeneration, Jinan University, Guangzhou 510632, China*
[2] *The Second Hospital of Jilin University, Changchun 130041, China*
[3] *Department of Otorhinolaryngology, The First Affiliated Hospital, Sun Yat-sen University, Guangzhou 510080, China*
[4] *Extracellular Vesicle Research and Clinical Translational Center, The First Affiliated Hospital, Sun Yat-sen University, Guangzhou 510080, China*
[5] *Central Laboratory of the Second Affiliated Hospital of Shandong First Medical University, Tai'an 271000, China*
[6] *Department of Human Anatomy, School of Medical, Jinan University, Guangzhou 510632, China*
[7] *Co-innovation Center of Neuroregeneration, Nantong University, Nantong 226019, China*
[8] *Neuroscience and Neurorehabilitation Institute, University of Health and Rehabilitation Sciences, Qingdao 266071, China*
[9] *Center for Exercise and Brain Science, School of Psychology, Shanghai University of Sport, Shanghai 200438, China*
§ *Fuxiang Li, Zhonghai Huang, and Jinrui Zhou contributed equally to this work.*

Cite this article: *Nano Research*, **2026**, *19*, 94908424. https://doi.org/10.26599/NR.2026.94908424

ABSTRACT: Neural repair following spinal cord injury (SCI) remains a significant medical challenge, necessitating effective therapeutic strategies. This study integrates mesenchymal stem cell-derived small extracellular vesicles (sEVs) with neurotrophin-3 (NT3) to generate NT3-loaded sEVs (NT3-sEVs) and evaluates their efficacy in acute SCI via intranasal delivery. Incorporation of NT3 significantly enhances sEV-mediated neurite outgrowth in cultured cortical neurons. In a mouse contusion SCI model, intranasal administration of NT3-sEVs over seven consecutive days results in superior functional recovery compared to sEV treatment alone, demonstrated by behavioral assessments, electrophysiological measurements, reduced lesion size, enhanced angiogenesis and axonal regeneration, inhibited glial activation, and preserved synaptic plasticity in lumbar motoneurons. Mechanistically, NT3-sEV administration activates the NT3-TrkC signaling pathway, increasing phosphorylation of downstream targets phospholipase C gamma (PLCγ), protein kinase C (PKC), and extracellular signal-regulated kinase (ERK), and upregulates proteins critical for axonal growth and neural plasticity (e.g., growth associated protein 43 (GAP43), synaptophysin, and microtubule associated protein 2 (MAP2)). Transcriptomic and proteomic analyses identify significant differential expression of genes and proteins involved in neural plasticity and immune modulation. Small RNA sequencing further reveals abundant miRNAs common to both sEVs and NT3-sEVs, likely suppressing neuroinflammatory and neuronal death pathways. Thus, intranasal delivery of NT3-sEVs offers a promising therapeutic strategy for SCI by modulating multiple targeted signaling pathways.

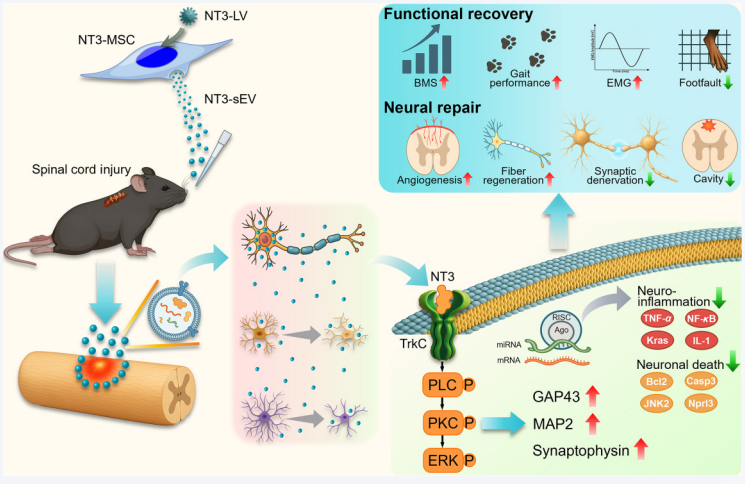

KEYWORDS: spinal cord injury, small extracellular vesicles, neurotrophin-3, intranasal administration, neural plasticity

Received: November 5, 2025; **Revised:** January 2, 2026; **Accepted:** January 9, 2026

✉Address correspondence to Libing Zhou, tlibingzh@jnu.edu.cn; Qing-Ling Fu, fuqingl@mail.sysu.edu.cn

1 Introduction

Spinal cord injury (SCI) is a severe disorder of the central nervous system (CNS), characterized by extremely limited self-healing capacity. Patients frequently suffer from permanent paralysis and functional disability, posing a significant global medical challenge [1]. Primary SCI induces disruption of the blood-spinal cord barrier and neural tissue, while secondary injury arises from neuroinflammation and oxidative stress, leading to edema, cavitation, and reactive gliosis [1, 2]. Descending inputs from supraspinal regions drive fine motor control and adaptive motor behaviors through direct and indirect connections with spinal motoneurons [3]. Clinically, approximately 67% of SCI cases involve incomplete injuries, with some residual fibers preserved even in the severe cases as demonstrated by imaging [4] and electrophysiological recording [5]. During the acute phase of SCI, alleviating secondary injury and promoting the neural plasticity of residual fibers are critical for facilitating subsequent functional recovery.

Mesenchymal stem cell (MSC) transplantation has been demonstrated to play beneficial roles in treating SCI [6]. However, its clinical translation faces several limitations, including low cell survival, immune rejection, and poor engraftment and homing — all of which hinder its effectiveness in acute SCI therapy [7]. Prior studies have shown that MSCs release abundant anti-inflammatory factors, cytokines, growth factors, and cell adhesion factors via paracrine, improving the lesion microenvironment and enhancing self-repair capacity [8]. Nevertheless, growing evidence suggests that small extracellular vesicles (sEVs) are key mediators of MSC paracrine effects [9].

sEVs constitute a heterogeneous group of cell-derived membranous structures comprising exosomes and microvesicles, which originate from the endosomal system or are shed from the plasma membrane, respectively [10]. Both prokaryotes and eukaryotes release sEVs, typically characterized by an average diameter of ~ 100 nm [11, 12]. sEVs are uniform lipid bilayer spheroids containing tetraspanin proteins as specific markers on their membranes [13, 14]. Their unique properties enable them to easily cross the blood-brain barrier (BBB) efficiently and protect cargo from denaturation [15–17]. sEVs encapsulate various substances, including DNA, RNA, lipids, metabolites, and cytosolic and cell-surface proteins [12], enabling intercellular communication and signal transduction [11, 18, 19].

Compared to MSCs, MSC-derived sEVs offer several advantages, such as non-cellular structure, low immunogenicity, natural drug delivery capability, and excellent tolerability [12, 15, 20, 21]. Furthermore, sEVs can be bioengineered to deliver therapeutic cargos for specific diseases [22–26], providing alternatives of stem cell therapies. Consequently, sEVs have emerged as ideal nanocarriers for drug delivery and targeted therapies, offering promising options beyond conventional stem cell therapy [15]. Numerous studies have demonstrated the therapeutic effects of MSC-derived sEVs in various neurological disorders [27], such as autism [28], stroke [29], traumatic brain injury [30, 31], Parkinson's disease [26], Alzheimer's disease [27, 32], and SCI [33]. Practically, the intranasal administration of sEVs represents an effective strategy for treating CNS pathologies [34]. This method offers multiple advantages: it is non-invasive, painless, simple, and enables rapid CNS entry with favorable tolerability [35]. Recent studies have shown that intranasal administration improves drug bioavailability in the CNS, allowing sEVs to traverse the BBB and migrate to the injured spinal cord area [33].

Neurotrophin-3 (NT3) belongs to the neurotrophic family, and is well known for restoring sensorimotor function in SCI rats by promoting axon growth and synaptic plasticity in multiple spinal pathways, including corticospinal tracts and proprioceptive pathways [36–39]. NT3 exerts its effects through growth stimulation and chemoattraction [36, 40]. However, its clinical use is challenged by suboptimal pharmacokinetics, limited systemic bioavailability, and its inability to cross the BBB [41].

This study aims to develop a combined therapeutic strategy for acute SCI by leveraging the complementary benefits of sEVs and NT3. We prepared NT3-loaded sEVs (NT3-sEVs) from cultured MSCs overexpressing NT3 and compared them with unmodified sEVs. First, we evaluated their ability to promote neurite outgrowth in cultured neurons. Then, using a contusion SCI mouse model [42], we studied the biodistribution of mCherry-sEVs *in vivo* after intranasal administration, compared the effects of intranasally-delivered sEV and NT3-sEV on functional recovery and neural structure repair, and elucidated the underlying mechanisms through Western blot analysis, transcriptomic and proteomic profiling of spinal cord samples, as well as small RNA sequencing of sEVs and NT3-sEVs combined with miRNA target prediction. Our findings indicate that intranasal administration of NT3-sEVs represents a promising therapeutic strategy for acute SCI, synergistically leveraging both the loaded NT3 protein and the highly abundant miRNAs in the vesicles.

2 Experimental

2.1 Preparation and characterization of NT3-sEVs

Preparation of MSCs derived from human urine epithelial cells-induced potential stem cells (iPSCs) has been previously described. Importantly, our MSCs exhibit near-immortalization characteristics, maintaining stable proliferation without significant senescence up to 50 passages [43]. This unique property renders them highly suitable for establishing stably transfected cell lines, facilitating sustained gene expression studies and therapeutic applications. To load NT3 and mCherry in sEVs, cultured MSCs were infected by NT3-lentivirus and mCherry-lentivirus LV-CMV-mCherry-WPRE-pA (BrainVTA, Wuhan, China) using polybrene (Hanbio, Shanghai, China) according to manufacturer's instructions. Cells (2×10^6 per dish) were seeded in two 15-cm cell culture dishes (NEST, Wuxi, Jiangsu, China) with the complete culture medium (CCM). After reaching 80% confluency, the medium was replaced with serum-free chemical defined medium media (CDPF) including CD-CHO (chemically defined chinese hamster ovary medium) (Gibco, Grand Island, NY, USA), hyaluronic acid and tocopherol (HT) supplement (Gibco, Grand Island, NY, USA), L-glutamine (Gibco, Grand Island, NY, USA), D-(+)-glucose (Sigma-Aldrich, St. Louis, MO, USA), non-essential amino acids (NEAA) (Gibco, Grand Island, NY, USA), and vitamin solution (Gibco, Grand Island, NY, USA). After 6 h, the medium was replaced with fresh CDPF medium. The conditioned medium was collected at 48 h and subjected to low-speed centrifugation (2000 *g*) for 10 min at 4 °C. Cell supernatants were harvested and followed by filtration using a 0.2-μm filter (Millipore, Burlington, MA, USA). sEVs were isolated using anion-exchange chromatography (AEC) kit (Mylab, Guangzhou, China) as describe [21]. The size of sEVs was determined by Nanoparticle tracking analysis (NTA, NanoSight NS300, Malvern Panalytical, Malvern,

UK); the characterization was studied by Western blots; the structure was observed by transmission electron microscopy (TEM, Hitachi, Tokyo, Japan). sEVs were aliquoted and stored at −80 °C immediately after preparation and were used within one month to ensure stability and activity.

2.2 Nano-flow cytometry-based permeabilization immunostaining

To evaluate NT3 loading efficiency and sub-vesicular localization in sEVs, nano-flow cytometry was performed using a NanoFCM analyzer (NanoFCMU30). Purified NT3-sEVs were incubated with 0.1% Triton X-100 (ELR00280, eLGbio; diluted in phosphate buffered saline (PBS)) or an equal volume of PBS (non-permeabilized control) at 37 °C for 30 min. Samples were then washed with PBS and concentrated using an ultrafiltration device (000351106, Merck). Next, sEVs were incubated with an anti-NT3 primary antibody (AB1532P, Merck; 20 ng/μL) at 4 °C for 30 min. After washing and concentration, sEVs were incubated with a fluorophore-conjugated secondary antibody (Goat Anti-Rabbit IgG H&L Alexa Fluor® 647, preadsorbed; ab150083, Abcam; 1:1000) at 37 °C for 30 min. Following a final wash and concentration step, labeled sEVs were acquired on the NanoFCM instrument. Blank and Triton-only blank controls were processed in parallel, and control sEVs were analyzed using the same staining and acquisition parameters.

2.3 Mouse contusion SCI model

All experimental procedures were strictly in line with the guidelines of the National Institutes of Health (NIH) Guide for the Care and Use of Laboratory Animals and approved by the Animal Ethics Committee of Jinan University (Approval No.: IACUC-20220407-01). C57BL/6 mice (18–22 g, 10 weeks old, female) were purchased from Beijing Vital River Laboratory Animal Technology Co., Ltd. and housed in a controlled environment with a temperature of 25 ± 1 °C, a relative humidity of 55% ± 10%, and 12-h light/dark cycles. Mice were randomly allocated into sham, control and experimental groups based on body weight and baseline motor function scores to ensure comparable injury severity and physiological conditions across groups. Mice in the sham group underwent laminectomy at the T9 level without spinal cord contusion and served as non-injured surgical controls. SCI mice were anesthetized with isoflurane and then underwent a contusive injury at T9 vertebral level using the Louisville Injury System Apparatus after laminectomy. The parameters were 0.5 mm in height, 1.0 m/s of contusion velocity and 0.4 s for a contact duration. Animals were excluded if their Basso Mouse Scale (BMS) scored more than 0 at day 1 after injury. All SCI mice were then randomly divided into three groups: the PBS, sEV, and NT3-sEV groups. Mice underwent twice daily bladder voiding care.

2.4 Intranasal administration

Intranasal delivery was performed using a standardized CNS-targeting protocol. Two hours after SCI, mice were fully anesthetized with isoflurane and placed in the standard dorsal recumbency position that facilitates direct nose-to-brain transport. To enhance nasal permeability, 5 μL hyaluronidase (20 U/μL, H3506, Sigma) was applied into each nostril with ~ 30-s intervals. 30 min later, EV suspensions were administered slowly at the nostril opening, allowing natural inhalation and complete absorption of each droplet before the next. This procedure was conducted once daily for 7 days.

2.5 Cortical neuron culture

After sterilization of newborn mice, cortical tissues were collected and cut into small pieces in the dissection medium (HBSS (Hank's balanced salt solution) plus 10 mM HEPES (4-(2-hydroxyethyl)piperazine-1-ethanesulfonic acid) and 1% Penicillin-Streptomycin). Samples were dissociated in 0.0125% trypsin-ethylenediaminetetraacetic acid (EDTA) (25200056, Gibco, USA) for 8 min at 37 °C and trypsinization was terminated by adding 10% fetal bovine serum (10082147, Gibco, USA) and DNase (11284932001, Roche, Swiss) solution for a 5-min incubation at room temperature. After a 5-min centrifugation, the cell suspension was filtered by a 70-μM cell strainer (352350, BD Falcon, Switzerland). Cells (9×10^5 per well) were seeded into poly-D-lysine (A3890401, Gibco, USA) coated coverslip in 12-well plates. The culture medium contained Neurobasal™-A Medium (A2477501, Gibco, USA), 2% B27 (17504001, Gibco, USA), 1% GlutaMAX™ Supplement (35050087, Gibco, USA), and 1% Penicillin-Streptomycin. Cells were cultured in an incubator at 37 °C and 5% CO_2. After 4–6 h of culture, the medium was replaced and 3×10^9 nanoparticles/well of sEVs and NT3-sEVs were added respectively. Cells were fixed by 4% paraformaldehyde for 30 min at days 3, 5, 7 *in vitro* (DIV) and followed by immunofluorescent staining. For sEV tracking study, 3×10^9 nanoparticles of mCherry-sEVs were added to the culture medium per well at 3 DIV and cells were fixed 24 h later for immunostaining using rabbit anti-β-Tubulin antibodies (1:1000; 2128, Cell Signaling Technology).

2.6 Pseudorabies virus (PRV) tracing

After isoflurane anesthetization, mouse sciatic nerves were exposed and 1 μL of PRV (1×10^9 plaque-forming units (PFU)/mL, P03001, BrainVTA, China) was injected into the nerve trunk using a 32-gauge Hamilton syringe. Animals were perfused by 4% paraformaldehyde 48 h later and lumbar spinal segments (L3–L5) were collected for preparing 30-μM frozen transverse sections, which were subjected to double immunostaining using mouse anti-synaptophysin (Syn, 1:1000, MAB5258, Millipore).

2.7 sEV tracing *in vivo*

To trace biodistribution of sEVs *in vivo*, mice were subjected to intranasal delivery of mCherry- sEVs (3.0×10^9 nanoparticles/time) immediately after SCI for 2 consecutive days (once a day). Twenty-four hours after the last administration, mice were perfused with 4% paraformaldehyde, and the tissues of brains and spinal cords were collected. Sagittal frozen sections (30-μM thickness) were immunostained using the following primary antibodies: rabbit anti-NeuN (1:1000; ab177487; Abcam), rabbit anti-Iba1 (1:1000; 019-19741; Wako) and rat anti-GFAP (1:1000; 13-0300; Thermo Fisher). Images were captured using confocal microscopy (LSM700; Carl Zeiss; Germany).

2.8 Enzyme-linked immunosorbent assay (ELISA)

The concentrations of NT3 were detected using an ELISA Kit (EH0245, FineTest, Wuhan, China) according to the manufacturer's instruction. In a 96-well microplate coated with monoclonal anti-NT3 antibody, 50 μL of NT3-sEVs or standard samples were mixed with 100 μL of horseradish peroxidase (HRP)-labelled secondary antibodies, and the microplate was kept at 37 °C for 60 min. After washing for 5 times, a 100-μL mixture of 0.01% H_2O_2 and 0.1% tetramethylbenzidine (1:1) was added for 15-min incubation at 37 °C. The reaction was stopped by adding 50 μL 2 M

H_2SO_4, and the absorbance at 450 nm was detected using chemiluminescence (Millipore, Bedford, MA, USA). This color reaction yielded a linear standard curve from 25–800 pg/mL. All experiments were performed 3 times.

2.9 Behavioral assessments

BMS scoring procedure: Mice were placed in an open field and observed for 5 min. The scoring system was based on hindlimb movement, including hind limb joint movement, weight support, plantar stepping, coordination, paw position, and trunk and tail control, and the criteria of BMS (0–9) were defined as below: 0–2, no to extensive ankle movement only; 3, paw placement (with or without weight support) or abnormal stepping patterns (dorsal stepping); 4–5, occasional to frequent plantar stepping with varying degrees of coordination and paw placement; 6–7, frequent plantar stepping (mostly coordinated with parallel paw placement and with varying degrees of trunk stability); 8, nearly normal stepping with mild trunk instability or normal stability and variable tail position; 9, completely normal locomotion with good trunk stability and tail consistently up.

2.10 Grid walking test

Animals were positioned on a square mesh metal grid (12 mm × 12 mm) to assess their skilled locomotor performance. Each mouse was placed in the center of the mesh grid for 5-min walking, and the percentage of hindlimb falling to total steps was counted.

2.11 Gait analysis

The gait performance was evaluated using a CatWalk analysis (XT9.1, Noldus, Netherlands), in which the main parameters included 30-cm walkway length, 20-s maximum run duration, and maximum 50% of run variation. Mice underwent 3-days pretraining to acclimate the environment. Each mouse was recorded at least 3 successful continuous runs, and parameters including print length, duty cycle (%), max contact max intensity, regularity index (%) were captured and analyzed. The system automatically initiated video recording triggered by mouse movement.

2.12 Electromyography (EMG) recordings

After animals were anesthetized with propofol (20 μL/g), a stimulating electrode was inserted into the ventral horn of T5 spinal segment after a laminectomy and a recording electrode was inserted into the gastrocnemius. EMG activity of the gastrocnemius muscle was recorded using the Nicolet VikingQuest EMG/EP System (Natus, USA), and the stimulation parameters were: 5000 mV pulse amplitude, 200 μs pulse duration, and a stimulation frequency of 1 Hz. EMG signal was filtered at a bandwidth of 30–3 kHz. In each animal, the recoding was repeated at least 6 times with an interval of 3 min.

2.13 Magnetic resonance imaging (MRI)

Animals were perfused with 4% paraformaldehyde at 8 weeks after SCI and spinal cords were dissected out followed by MRI scanning using a 9.4 T MRI scanner (Bruker BioSpin 94/30USR, Ettlingen, Germany). T2-weighted images were captured at the sagittal, transverse, coronal views. The acquisition parameters were time of repetition/time of echo (TR/TE) = 3000/20 ms, fractional anisotropy (FA) = 180, matrix size = 196 × 196 (a), field of view (FOV) = 10 × 10 mm^2, thickness/gap = 0.7/0 mm, the slice numbers were 19, 3 and 3 at the sagittal, transverse, coronal views respectively. Serial sections were exported, and residual tissue volume (mm^3) and lesion cavity volume (mm^3) were calculated using ImageJ software. The atrophy rate was presented as the ratio of cavity volume to residual volume.

2.14 Immunofluorescent staining

Floating method was used for routine immunofluorescent staining. Briefly, sections were washed with 0.01M PBS plus 0.3% Triton, blocked in a solution containing 3% bovine serum albumin plus 10% normal donkey serum for 2 h. Sections were then incubated with primary antibodies overnight at 4 °C, which included rabbit anti-NeuN (1:1000; ab177487, Abcam), rabbit anti-Iba1 (1:1000; 019-19741, Wako), rat anti-CD68 (1:1000; ab53444; Abcam), rat anti-GFAP (1:1000; 13-0300; Thermo Fisher), rabbit anti-serotonin (5-HT, 1:1000, S5545, Sigma), mouse anti-CD31 (1:500; sc-376,764; Santa cruz), rabbit anti-microtubule-associated Protein 2 (MAP2, 1:1000, ab5622, Millipore), mouse anti-synaptophysin (Syn, 1:1000, MAB5258, Millipore). Signal was revealed using fluorescent Alexa Fluor 488 or 594 secondary antibodies (1:1000; A21206/A11012/A11007/A11006/A32744, Thermo Fisher). After staining, sections were rinsed three times in 0.01 M PBS and mounted on glass slides with antifade mounting medium (F4680, Sigma). Images were scanned by a confocal microscope (LSM700; Carl Zeiss; Germany).

2.15 Western blotting

Spinal cord samples were collected 7 days after SCI for Western blot analysis. Tissues were lysed on ice for 30 min in Radioimmunoprecipitation assay (RIPA) buffer lysis and extraction buffer (Thermo Fisher Scientific, USA) supplemented with 1 mM protease and phosphatase inhibitor cocktail (Thermo Fisher Scientific, USA). Samples were briefly homogenized by ultrasonication. Lysates were clarified by centrifugation at 12,000 rpm for 20 min, and protein concentrations were determined using a bicinchoninic acid (BCA) Protein Assay Kit (Thermo Fisher Scientific, USA). Equal amounts of protein were separated by 10% or 12% sodium dodecyl sulfate-polyacrylamide gel electrophoresis (SDS-PAGE) and transferred onto polyvinylidene fluoride (PVDF) membranes (Sigma-Aldrich, USA) by electroblotting. Membranes were blocked with 5% nonfat milk in Tris-buffered saline with Tween-20 (TBST) for 2 h at room temperature and incubated overnight at 4 °C with the following primary antibodies: rabbit anti-TrkC (1:1000, Cell Signaling Technology, USA), rabbit anti-phospho-Tyr490 (1:1000, Cell Signaling Technology, USA), rabbit anti-GAPDH (1:1000, Cell Signaling Technology, USA), rabbit anti-PLCγ (1:1000, Cell Signaling Technology, USA), rabbit anti-phospho-PLCγ (1:1000, Cell Signaling Technology, USA), rabbit anti-PKC (1:1000, Cell Signaling Technology, USA), mouse anti-phospho-PKC (1:1000, Santa Cruz, USA), rabbit anti-NMDA receptor 1 (1:1000, Cell Signaling Technology, USA), rabbit anti-ERK (1:1000, Cell Signaling Technology, USA), rabbit anti-phospho-ERK (1:1000, Cell Signaling Technology, USA), rabbit anti-GAP43 (1:1000, Abcam, UK), rabbit anti-MAP2 (1:1000, Cell Signaling Technology, USA), and mouse anti-synaptophysin (1:5000, GeneTex, USA). After washing, membranes were incubated with the appropriate HRP-conjugated secondary antibodies for 2 h at room temperature. Signals were developed using enhanced chemiluminescence (ECL) reagent (Merck Millipore, USA), captured with a ChemiDoc Imaging System (Bio-Rad, USA), and quantified using ImageJ software (National Institutes of Health, USA).

2.16 RNA-sequencing (RNA-seq) analysis of spinal cord samples

Total RNA was extracted from fresh spinal cord tissues (T7-T11 segments) after 7 days of SCI using TRIzol reagent, and cDNA was synthesized from purified mRNA of each sample to construct libraries. RNA quality was assessed by agarose gel electrophoresis, NanoDrop spectrophotometry, and Agilent 2100 analysis. Samples with clear 28S and 18S rRNA bands, OD260/280 between 1.8–2.1, and RNA integrity number (RIN) ≥ 7.0 were considered of sufficient quality for RNA-seq. The sequencing was performed on the Illumina NovaSeq X Plus platform. Raw reads were filtered (fastp v0.18.0: removal of adapters, $Q < 20$ bases, ambiguous nucleotides), followed by rRNA depletion (Bowtie2 v2.2.8). Clean reads were aligned to the reference genome (HISAT2 v2.1.0), and transcript abundances (FPKM/TPM (fragments per kilobase of transcript per million fragments mapped/transcripts per million)) were quantified using StringTie v1.3.1 and RSEM. Differential gene expression analysis was performed with DESeq2, identifying genes with a false discovery rate (FDR) < 0.05 and $|\log_2\text{Fold change}| > 1.5$. Functional enrichment analyses (Gene Ontology (GO), Kyoto Encyclopedia of Genes and Genomes (KEGG)) were conducted using hypergeometric tests (FDR ≤ 0.05) to uncover biological pathways and disease associations. Sample reproducibility and variance were assessed via principal component analysis (PCA) and correlation analysis. Advanced investigations included protein–protein interaction network construction (STRING v10, visualized in Cytoscape v3.7.1), global pathway exploration via Gene Set Enrichment Analysis (GSEA), and Reactome pathway analysis.

2.17 Proteomics analysis

Seven days after SCI, fresh spinal samples (T7–T11 segments) were collected for proteomic analysis at the Gene Denovo Biotechnology Company (Guangzhou, China). Briefly, tissues were homogenized in the lysis buffer (2% SDS, 7 M urea, 1 mg/mL protease inhibitor cocktail) for 3 min on ice using an ultrasonic homogenizer, and the supernatants were collected after centrifugation at 14,000 rpm for 15 min at 4 °C. The protein concentration was measured using a BCA Protein Assay Kit. Proteins were digested with sequence-grade modified trypsin (Promega, Madison, WI) at a substrate/enzyme ratio of 50:1 (w/w) at 37 °C for 16 h and then subjected to high pH reverse phase separation using the Ultimate 3000 system (ThermoFisher Scientific, MA, USA) connected to a reverse phase column (Waters Corporation, MA, USA). Protein quality and reproducibility among replicates were evaluated using SDS-PAGE. Samples exhibiting sharp, clearly defined bands with minimal smearing were considered of high quality. Reproducibility was confirmed by the high similarity in band patterns across biological replicates. After fractions were collected and dried, they were performed for nano-HPLC-MS/MS analysis using on-line nanospray LC-MS/MS on an Orbitrap Fusion Lumos coupled to EASY-nLC 1200 system (Thermo Fisher Scientific, MA, USA). The mass spectrometer was operated under data independent acquisition (DIA) mode, automatically switched between mass spectrometry (MS) and MS/MS mode. Raw data of DIA were processed and analyzed by Spectronaut X (Biognosys AG, Switzerland) with default parameters. Different expressed proteins (DEPs) were considered with a P value (FDR) < 0.05 and $|\log_2\text{Fold change}| > 0.58$. The protein function and classification were analyzed using the following database: GO and KEGG. GESA was performed by software GSEA and MSigDB to identify a set of genes in specific GO terms/pathways with significant differences, enrichment scores and P value were calculated in default parameters. In each group, 3 animals were used.

2.18 Small RNA-seq analysis of sEVs

Total RNA was extracted from sEVs and NT3-sEVs using TRIzol reagent, and small RNAs (18–30 nt) were size-selected via PAGE. Libraries were constructed through 3' and 5' adapter ligation, reverse transcription, and PCR amplification, followed by Illumina NovaSeq X Plus sequencing. Raw reads were filtered to remove adapters, low-quality bases ($Q \leq 20$), polyA sequences, and fragments < 18 nt. Clean reads were aligned to GenBank (v209.0) and Rfam (v11.0) to exclude non-coding RNAs (rRNA, tRNA, etc.), then mapped to the human genome to filter exon-, intron-, and repeat-associated sequences. Known miRNAs were identified via miRBase (v22), while novel miRNAs were predicted using miRDeep2 (default parameters). miRNA expression was normalized to TPM. Differential analysis ($|\log_2\text{Fold change}| > 2$, $P < 0.05$) between sEV and NT3-sEV groups was performed with edgeR. Target genes of DE miRNAs were predicted using TargetScan v7.0 and miRanda v3.3a (strict seed pairing, energy thresholds). Functional enrichment (GO/KEGG, hypergeometric test, FDR ≤ 0.05) and miRNA-specific analyses (clusters < 10 kb, base editing, family conservation) were conducted.

2.19 Statistical analysis

All data were presented as mean ± standard error of the mean (SEM) and analyzed by GraphPad Prism 8.0.2 (La Jolla, USA). Comparisons between the experimental groups were performed by one-way ANOVA or two-way ANOVA with Tukey's post-hoc test. $P < 0.05$ was considered statistically significant.

3 Results

3.1 NT3-sEVs are successfully harvested from NT3-overpressed MSCs

Using anion exchange chromatography, we prepared high-quality sEVs from MSCs as previously described [21, 44]. To overexpress NT3 in MSCs (termed NT3-MSCs), the NT3 sequence was cloned into a lentiviral vector (LV) plasmid (LV-EF1a-3XFlag-NTF3-P2A-EGFP-PGK-Puro-WPRE), which was amplified in HEK293F cells. The purified, NT3-containing lentivirus was then used to infect MSCs (Fig. 1(a)). MSCs cultured without transfection served as controls for sEV preparation. The conditional medium was collected to purify sEVs using anion exchange chromatography (Fig. 1(a)). Lentivirus-transfected MSCs proliferated normally, with most cells expressing green fluorescent protein (GFP), which was co-expressed from the plasmid (Fig. 1(b)).

Nanoparticle tracking analysis showed peak diameters of 118 nm for sEVs and 93 nm for NT3-sEVs, with concentrations of 1.338×10^{11} (sEVs) and 2.396×10^{11} (NT3-sEVs) particles/mL, respectively (Fig. 1(c)). Both exhibited typical bilipid-layered morphology under transmission electron microscopy (Fig. 1(d)). To further assess whether NT3 loading alters the physicochemical properties of MSC-derived sEVs, ZetaView analysis was performed. As shown in Fig. S1 in the Electronic Supplementary Material (ESM), MSC-sEVs and NT3-MSC-sEVs displayed highly comparable ζ-potential profiles, with mean ζ-potentials of approximately −33.74 and

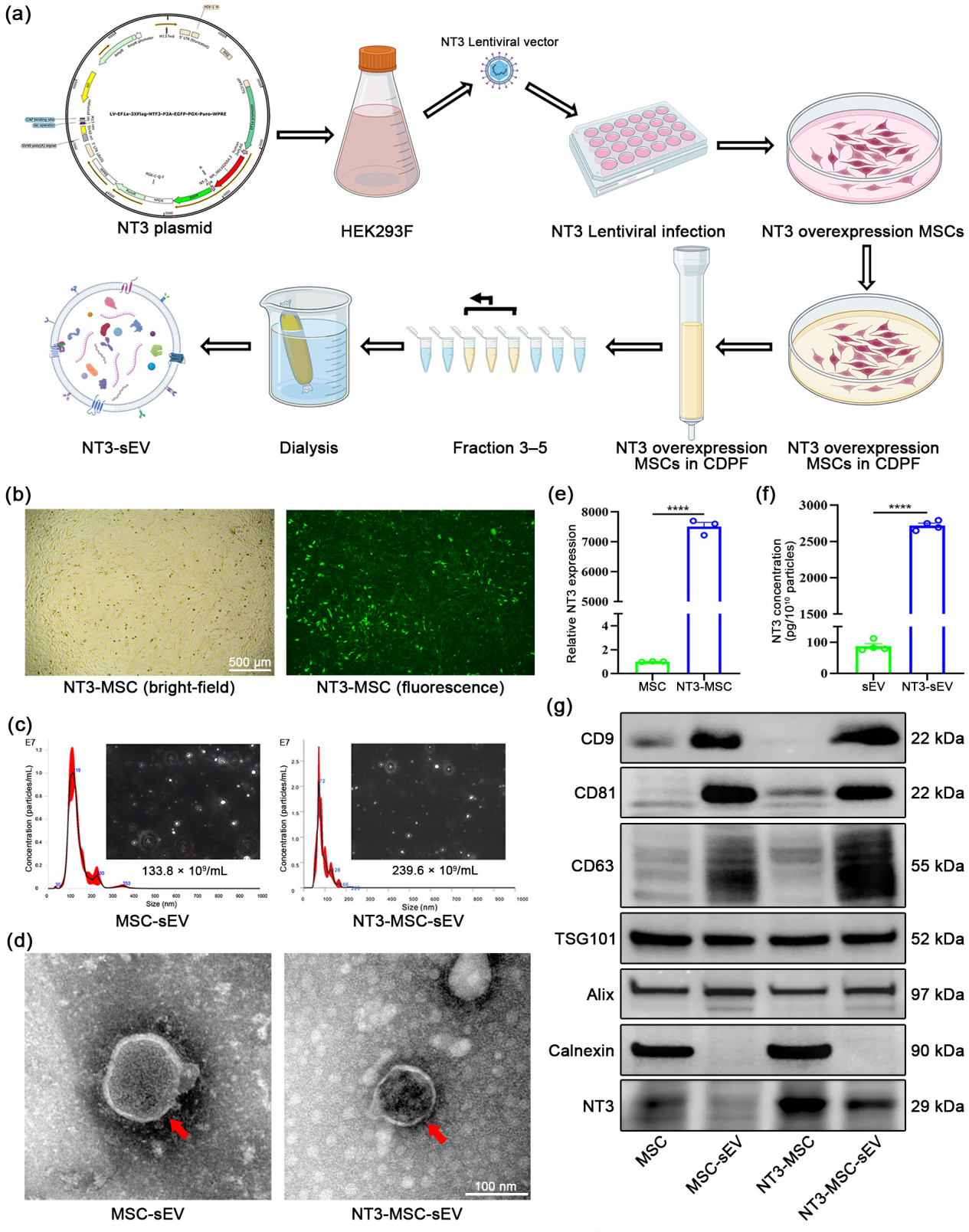

Figure 1 Preparation and characterization of NT3-sEVs. (a) The diagram of the preparation and purification of NT3-sEVs from NT3-overexpressing MSCs. (b) Images of NT3-LV-transfected MSCs under bright-field microscopy (left) and fluorescent microscopy (right) under which transfected MSCs were visualized by GFP. (c) NTA showing the size distribution of sEVs from MSCs (MSC-sEV) and NT3-overexpressing MSCs (NT3-MSC-sEV). (d) MSC-sEV and NT3-MSC-sEV containing the typical vesicle membrane under transmission electron microscope. A significant increase of NT3 mRNA in NT3-overexpressing MSCs (NT3-MSCs) confirmed by (e) RT-qPCR and of NT3 proteins in NT3-sEVs identified by (f) ELISA. $^{****}P < 0.0001$, one-way ANOVA, $n = 3$ independent experiments. (g) Western blots showing that sEVs (MSC-sEV) and NT3-sEVs (NT3-MSC-sEV) are positive for CD9, CD81, and CD63 but negative for Calnexin, and that there is a significant increase of NT3 proteins in NT3-MSCs and NT3-MSC-sEVs.

−34.96 mV, respectively, and similar distribution widths (21.12 vs. 24.63 mV) (Figs. S1(a) and S1(b) in the ESM). The close overlap in both peak position and distribution spread indicates that NT3 overexpression does not affect the surface charge or electrostatic properties of MSC-derived sEVs. In addition, ZetaView measurements revealed comparable particle concentration, tracking quality, and signal stability between the two groups, further supporting that NT3 loading does not compromise vesicle integrity, membrane stability, or overall physicochemical characteristics. To further determine the loading efficiency and sub-vesicular localization of NT3, nano-flow cytometry analysis was performed (Fig. S2 in the ESM). Under blank conditions, no detectable fluorescence signal either in the absence (Fig. S2(a) in the ESM) or presence (Fig. S2(b) in the ESM) of 0.1% Triton X-100, confirming minimal background fluorescence. Upon NT3 immunostaining without membrane permeabilization (Fig. S2(c) in the ESM), NT3-sEVs displayed a low proportion of NT3-positive particles (~ 4.6%), whereas membrane permeabilization with 0.1% Triton X-100 (Fig. S2(d) in the ESM) markedly increased NT3-positive events to ~ 47.0%, accompanied by enhanced fluorescence intensity, indicating that NT3 is predominantly localized within the lumen of NT3-sEVs rather than present as surface-associated or free extracellular protein.

Consistently, NT3 mRNA level was significantly elevated in NT3-MSCs compared to controls (Fig. 1(e)) and ELISA quantification revealed a robust increase in NT3 protein levels in NT3-sEVs (2650 ± 62.88 pg/10^{10} nanoparticles; Fig. 1(f)). In Western blots, sEVs and NT3-sEVs were positive for CD9, CD81 and CD63 (specific markers for sEVs) but negative for Calnexin which was specifically expressed by MSCs, and strong NT3-positive signal was identified in NT3-MSCs and NT3-sEVs (Fig. 1(g)). Thus, NT3 was successfully loaded into sEVs by overexpressing NT3 in MSCs, and NT3-sEVs retained morphological and molecular characteristics similar to unmodified sEVs.

3.2 NT3-sEVs promote neurite outgrowth of cultured cortical neurons more effectively than sEVs

We tracked sEV distribution in 3-day-*in-vitro* (DIV) cultured primary cortical neurons by adding mCherry-sEVs to the culture medium. After 12 h, mCherry-labelled nanoparticles were readily identified in neurons via anti-Tuj1 immunofluorescent staining (Fig. S3(a) in the ESM). To evaluate the effect of sEVs and NT3-sEVs on neurite outgrowth, cultured neurons were treated with 3 × 10^9 nanoparticles of sEVs (sEV group) or NT3-sEVs (NT3-sEV group), or an equivalent volume of PBS (PBS group) to 500-μL culture medium at 1 DIV. Cultured neurons were fixed and stained with anti-Map2 antibodies at 3, 5 and 7 DIV, respectively (Fig. S3(b) in the ESM). Neuronal branches were significantly increased in both the sEV and NT3-sEV groups compared to the PBS group at all timepoints, with a greater number of branches observed in the NT3-sEV group than the sEV group at 5 and 7 DIV (Fig. S3(c) in the ESM). Analysis of total neurite length revealed a significant increase in the sEV group at 5 and 7 DIV, and in the NT3-sEV group at all three timepoints compared to the PBS group, with significantly greater increase in the NT3-sEV group than in the sEV group (Fig. S3(d) in the ESM). These results suggest that both sEVs and NT3-sEVs efficiently promote neurite outgrowth and branching, with NT3-sEVs showing superior efficacy.

3.3 Intranasally delivered NT3-sEVs more effectively facilitate functional improvement in SCI mice than sEVs

Using a contusion SCI mouse model targeting the T9 segment, we first investigated the biodistribution of intranasally-delivered mCherry-sEVs *in vivo* (Fig. S4(a) in the ESM). After 24 h of administration, abundant mCherry-labelled nanoparticles were observed in the olfactory bulb, cortex, and spinal cord, with much overlapping with NeuN-positive neurons (Fig. S4(c): c1–c3 in the ESM). Transverse spinal sections adjacent to the lesion (Fig. S4(d) in the ESM) were subjected to immunofluorescent staining against NeuN, Iba1 and glial fiber acid protein (GFAP) to identify sEV distribution in different cell types. A large number of mCherry-labelled nanoparticles surrounded NeuN-positive nuclei of spinal neurons indicating their uptake by neurons (Fig. S4(e) in the ESM). Anti-Iba1 immunostaining revealed reactive microglia around the lesion with hypertrophied cell bodies and short, thick processes, with some overlap between mCherry-labeled nanoparticles and Iba1-positive microglia (Fig. S4(f) in the ESM). Similarly, reactive astrocytes identified by anti-GFAP immunostaining surrounded the lesion but rarely overlapped with mCherry-labeled nanoparticles (Fig. S4(g) in the ESM). Statistical analysis showed significant differences in sEV uptake among three types of spinal cells (Fig. S4(b) in the ESM): high in neurons (93.06% ± 3.067%), low in microglia (34.36% ± 9.706%) and astrocytes (9.835% ± 3.353%). These results indicate that sEVs can be efficiently transported to the brain and spinal cord of SCI mice after intranasal administration and are predominantly taken up by neurons. In contrast, fluorescence analysis of major peripheral organs, including the lung, heart, liver, kidney, and spleen, showed no detectable mCherry signal at the same time point (data not show), indicating minimal pulmonary or systemic accumulation and supporting the CNS-preferential distribution of intranasally administered sEVs.

To evaluate the therapeutic efficacy of sEVs and NT3-sEVs, SCI mice were randomly divided into three groups and received daily intranasal administrations of sEVs or NT3-sEVs at a dose of 3 × 10^9 nanoparticles per mouse per day, or an equivalent volume of PBS (PBS group), for 7 consecutive days post-SCI. A sham group, which underwent laminectomy without spinal cord contusion, was included as a non-injured control (Fig. 2(a)). The body weight of all mice gradually decreased during first 3 days after SCI and then gradually recovered, with no differences in three groups (Fig. 2(b)). Behavioral performance was assessed using BMS scores before and weekly after SCI (Fig. 2(c)). Sham mice consistently maintained maximal BMS scores, confirming intact motor function. BMS scores increased in the first two weeks in all four groups and became relatively stable in the PBS group while continuing to increase in the sEV and NT3-sEV groups thereafter (Fig. 2(d)). Compared to the PBS group, BMS scores were significantly higher in the sEV group from days 28 to 56 and in the NT3-sEV group from days 7 to 56, with significant differences between the NT3-sEV group (higher) and the sEV group (lower) from days 21 to 56 (Fig. 2(d)). Walking balance was assessed using footfault tests (Fig. 2(e)). Sham mice showed minimal footfaults throughout the experiment. In contrast, SCI mice exhibited marked impairments, which were significantly alleviated in the sEV group from days 42 to 56 and in the NT3-sEV group from days 28 to 56 compared with the PBS group (Fig. 2(f)).

At day 42 post-SCI, Catwalk gait analysis was performed to

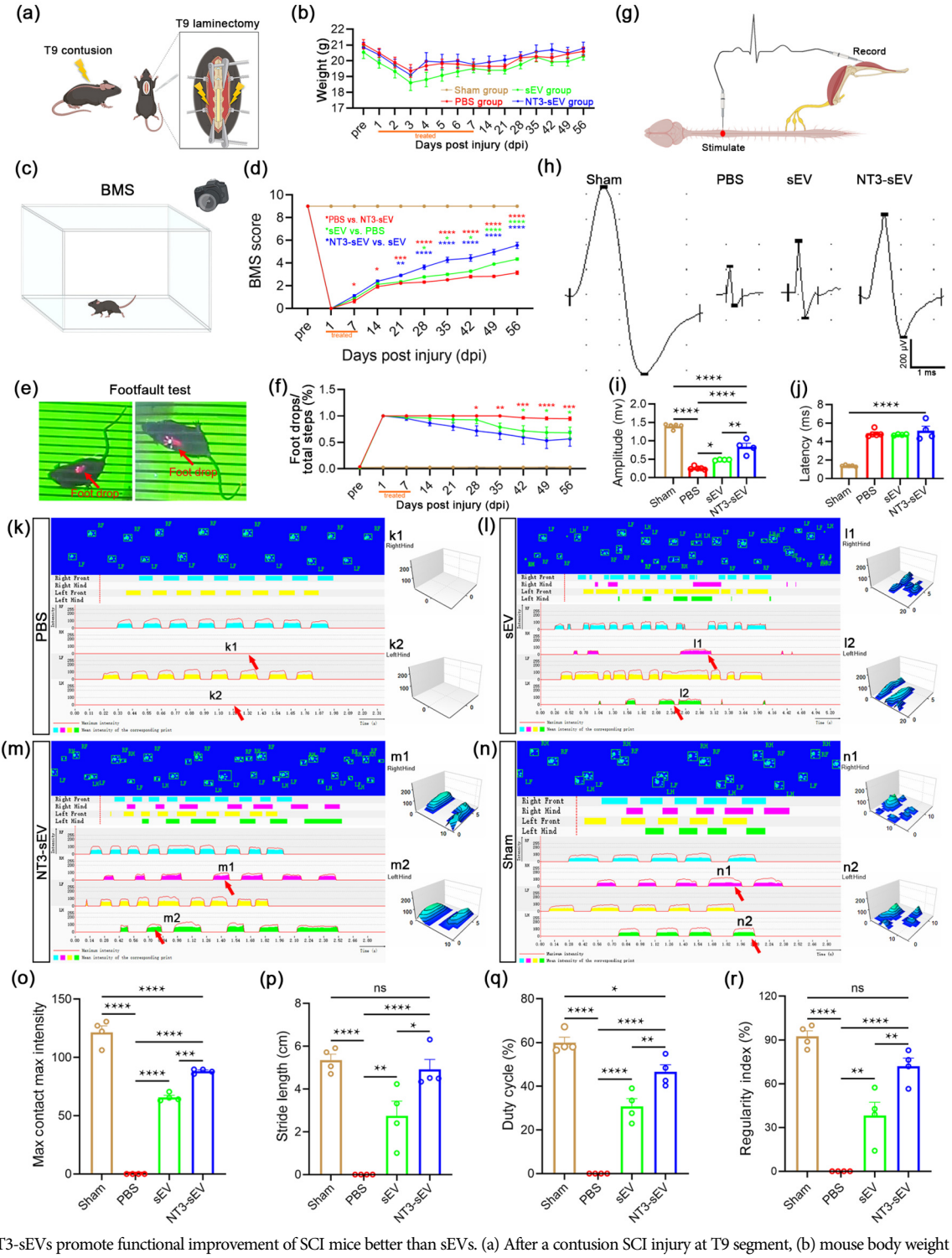

Figure 2 NT3-sEVs promote functional improvement of SCI mice better than sEVs. (a) After a contusion SCI injury at T9 segment, (b) mouse body weight decreased in the first 3 days and then gradually recovered, with no significant differences in three groups (PBS: $n = 10$, sEV: $n = 8$, NT3-sEV: $n = 9$). (c) BMS scores were dynamically assessed post-SCI, (d) showing a significant increase in the sEV and NT3-sEV groups compared to the PBS group and higher scores in the NT3-sEV group than the sEV group (PBS: $n = 10$, sEV: $n = 8$, NT3-sEV: $n = 9$, Sham: $n = 6$). Red star: NT3-sEV vs. PBS; green star: sEV vs. PBS; blue star: NT3-sEV vs. sEV. (e) Footfault tests showed that sham mice exhibited minimal slipping steps, whereas (f) the percentage of slipping steps was significantly decreased in the sEV and NT3-sEV groups compared to the PBS group ($n = 6$ per group). Red star: NT3-sEV vs. PBS; green star: sEV vs. PBS. (g, h) EMG of gastrocnemius was recorded upon stimulating spinal cord. Sham mice displayed robust EMG responses. (i) The amplitude was significantly increased in the sEV and NT3-sEV groups compared to the PBS group, with a greater increase in the NT3-sEV group than the sEV group, whereas (j) latency was comparable among the SCI groups. At day 42 post-SCI, mice underwent CatWalk gait analysis to record hindpaw footprints and gait performance in the (k) PBS, (l) sEV, (m) NT3-sEV, and (n) sham groups. Representative footprint patterns and tri-dimensional footprint intensity maps of hindlimbs are shown (k1, k2; l1, l2; m1, m2; n1, n2). Quantitative analysis revealed significant increases in maximal (o) contact intensity, (p) stride length, (q) duty cycle, and (r) regularity index in the sEV and NT3-sEV groups compared to the PBS group, with more pronounced improvements in the NT3-sEV group. Sham mice exhibited normal gait parameters. $^{*}P < 0.05$; $^{**}P < 0.01$; $^{***}P < 0.0005$; $^{****}P < 0.0001$; one-way ANOVA multiple comparison and Tukey post hoc.

further assess hindpaw footprint and gait performance among the four groups. Sham mice displayed normal, continuous hindpaw footprints and stable gait parameters (Fig. 2(n)). In contrast, hindpaw footprints were rarely detectable in the PBS group but were clearly visualized in the sEV and NT3-sEV groups (Figs. 2(k)–2(m)). The maximal contact intensity of hindpaws was significantly higher in the NT3-sEV group (88.25 ± 1.88) than in the sEV group (66.78 ± 3.348) (Fig. 2(o)), indicating enhanced weight-bearing capacity in the NT3-sEV group. Stride length was significantly increased in the NT3-sEV group (4.913 ± 0.932 cm) compared to the sEV group (2.741 ± 1.376 cm) (Fig. 2(p)). The duty cycle (%) calculated as the percentage of time that the hindlimb supported during the walking cycle, was significantly higher in the NT3-sEV group (46.54 ± 6.528) than in the sEV group (30.79 ± 6.995) (Fig. 2(q)). The Regularity Index of hindpaws was higher in the NT3-sEV group (71.95 ± 11.24) than in the sEV group (38.29 ± 17.99) (Fig. 2(r)), reflecting better coordination of hindlimbs in the NT3-sEV group. In contrast, all these parameters of Catwalk tests were undetectable in the PBS group (Figs. 2(o)–2(r)). These parameters in the NT3-sEV group approached, but did not fully reach, the levels observed in sham mice.

Before sacrifice, EMG recordings of gastrocnemius muscle were conducted upon stimulating the spinal cord above the lesion (Figs. 2(g) and 2(h)). Sham mice exhibited robust and stable EMG responses (1.400 ± 0.068 mV), whereas SCI markedly reduced EMG amplitude in the PBS group (0.258 ± 0.044 mV). The amplitude was significantly increased in the sEV group (0.483 ± 0.013 mV) and NT3-sEV group (0.837 ± 0.195 mV) compared to the PBS (Fig. 2(i)). No significant differences in latency were observed among the SCI groups, while sham mice displayed consistently shorter and stable latencies (Fig. 2(j)).

Collectively, these results indicate that administration of both sEVs and NT3-sEVs effectively contributes to functional improvement in SCI mice, with NT3-sEVs exhibiting superior therapeutic effects compared to sEVs.

3.4 NT3-sEV and sEV administration reduces lesion cavities and fosters tissue preservation in injured spinal cords

The lesion cavity is a hallmark pathological feature at the subacute and chronic stages of SCI. Fifty-six days post-SCI, animals were perfused, and entire spinal cords were dissected. The lesion was clearly identifiable in all groups (Fig. 3(a)). We performed MRI scanning of the injured spinal cords including the lesion epicenter and its rostral and caudal segments. In T2-weighted images, we quantified the areas of residual tissue and lesion areas at different levels (Fig. 3(b)). Compared to the PBS group, the areas of preserved tissues were significantly increased in the caudal regions (−2.1, −1.4, −0.7 mm) and the lesion center in the sEV group, as well as at all levels in the NT3-sEV group; the preserved tissue areas were larger in the regions 2.1 mm rostral and caudal to the lesion center in the NT3-sEV group compared to the sEV group (Fig. 3(c)). The ratios of lesion area to preserved tissue area were significantly decreased from −1.4 mm (rostral) to 1.4 mm (caudal) in the sEV group, and from −1.4 to 2.1 mm in the NT3-sEV group compared to the PBS group, with the lesion epicenter defined as 0 mm (Fig. 3(d)). These findings demonstrate that both NT3-sEV and sEV administration effectively reduce lesion cavity formation and promote tissue preservation after SCI, with NT3-sEVs exhibiting superior efficacy compared to sEVs.

3.5 Administration of NT3-sEV and sEV promotes angiogenesis after SCI

SCI results in the interruption of blood supply in the injured region, and angiogenesis facilitates the reconstruction of collateral circulation, which is beneficial for neural repair. To investigate the effects of intranasally-delivered NT3-sEVs and sEVs on angiogenesis, sagittal spinal sections at 56 days post-SCI were immunostained with an anti-CD31 antibody, a marker for endothelial cells. CD31-positive cells were readily identified in the lesion center and surroundings in the PBS group (Figs. 3(e), 3(e1), and 3(e2)), the sEV group (Figs. 3(f), 3(f1), and 3(f2)) and the NT3-sEV group (Figs. 3(g), 3(g1), and 3(g2)). Statistical analysis revealed a significant increase of cell density in both the NT3-sEV group (62.06 ± 5.479 cells/mm^2) and the sEV group (50.00 ± 4.704 cells/mm^2) compared to the PBS group (34.81 ± 7.392 cells/mm^2), with a significantly greater increase observed in the NT3-sEV group than in the sEV group (Fig. 3(h)).

3.6 NT3-sEV administration promotes serotonergic axon regeneration after SCI

Serotonergic fibers primarily originate from the raphe nuclei and form extensive synapses with spinal neurons across different spinal cord segments. Previous studies have demonstrated that SCI damages the descending serotonergic fibers projecting from the brainstem to the spinal cord. However, enhancing serotonin (5-HT) levels may contribute to functional recovery, highlighting the potential of serotonergic replacement strategies in promoting locomotor rehabilitation [45, 46]. To investigate whether intranasal administration of sEVs and NT3-sEVs fosters serotonergic axon regeneration, we collected thoracic spinal segments at 56 days post-SCI and performed anti-5-HT immunostaining in sagittal sections (Figs. 3(i)–3(k)). A great number of 5-HT-positive fibers were present in the rostral region, with some in the lesion and few in the caudal region (Figs. 3(i)–3(k)). We counted axons at different transverse panels spanning the lesion center (defined as 0 μm), rostral and caudal regions and found a significant increase in 5-HT-positive fibers in the caudal region and lesion center in the NT3-sEV group compared to the PBS group (Fig. 3(l)). Although there was an increase trend in axon number in the sEV group compared to the PBS group, no significant differences were observed between these two groups (Fig. 3(l)). These findings indicate that intranasal administration of NT3-sEVs effectively promotes axon regeneration and/or delays axon degeneration after SCI.

3.7 Intranasal administration of NT3-sEVs and sEVs enhances synaptic plasticity of lumbar motoneurons after SCI

Hindlimb locomotion is directly driven by lumbar spinal motoneurons, and SCI at thoracic spinal segments in our study interrupted supraspinal and propriospinal inputs to spinal motoneurons below the lesion. To assess this, synaptic changes on lumbar spinal motoneurons were evaluated. PRV was injected into the sciatic nerves at 53 days post-SCI to retrogradely label lumbar motoneurons, and L3–L5 spinal segments were collected 3 days later (Fig. 4(d)). Transverse spinal sections were immunostained with anti-Synaptophysin (a maker for presynaptic vesicles). In the ventral horn, lumbar spinal motoneurons were well traced by PRV, with their somas and neurites visible in all groups (Figs. 4(a)–4(c)).

The average numbers of PRV-labeled motoneurons were

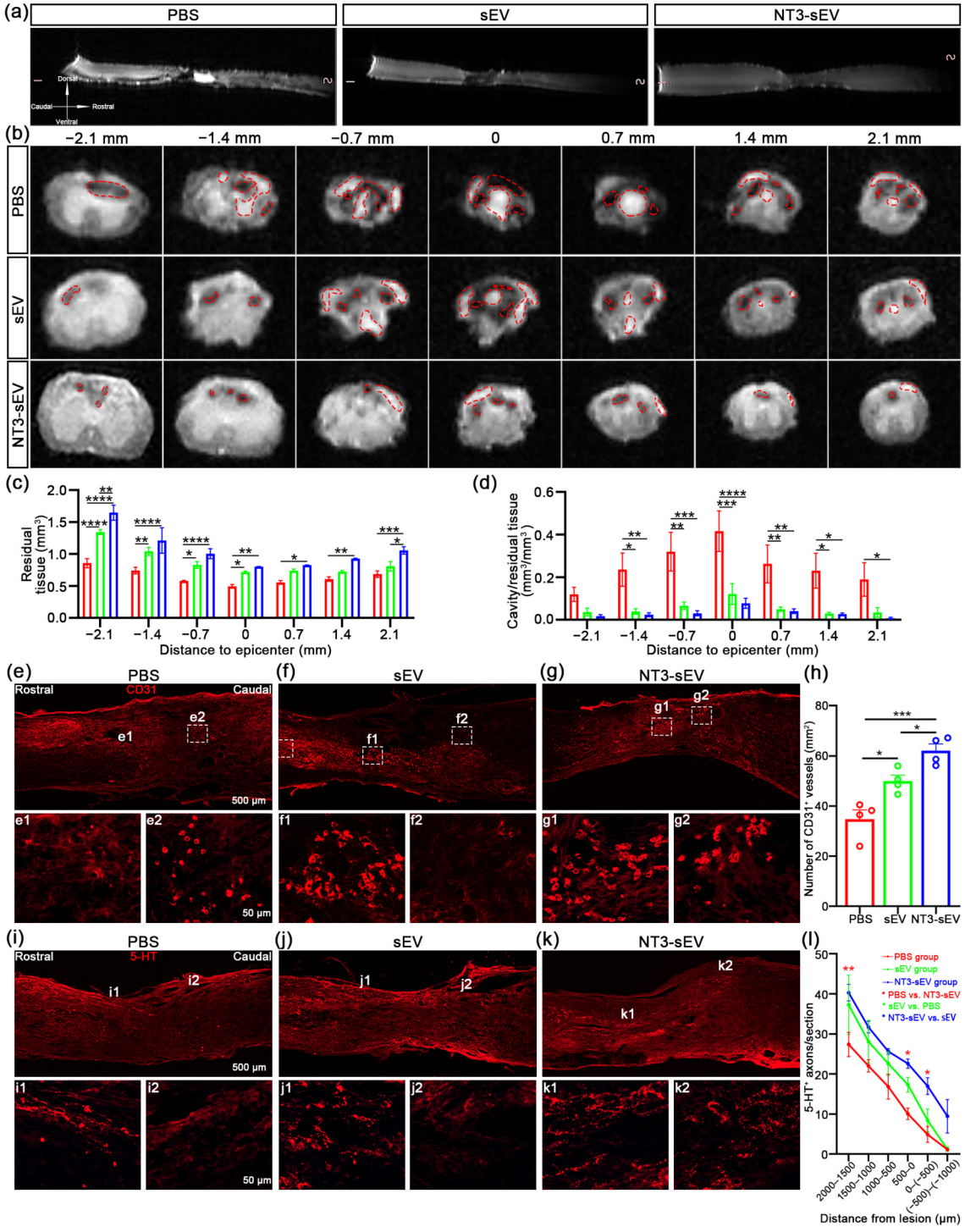

Figure 3 NT3-sEVs superiorly facilitates structure repair of injured spinal cords than sEVs. At day 56 post-SCI, animals were perfused, and spinal cords were collected for structural analysis: (a) T2-weighted sagittal MRI images clearly showed the lesion location in each group. (b) T2-weighted transverse MRI images were acquired at the lesion epicenter (0 mm), and multiple rostral and caudal levels. (c) Quantification of preserved tissue areas demonstrated significant increases in the sEV group (−2.1, −1.4, −0.7, and 0 mm) and in the NT3-sEV group at all examined levels compared with PBS. Moreover, the NT3-sEV group showed larger preserved tissue areas at 2.1 mm rostral and caudal to the lesion center compared with the sEV group. (d) The ratios of lesion area to preserved tissue area were significantly reduced in the sEV group from −1.4 mm rostral to 1.4 mm caudal, and in the NT3-sEV group from −1.4 mm rostral to 2.1 mm caudal, relative to the PBS group. The lesion epicenter was defined as 0 mm for uniform level comparison. Anti-CD31 immunofluorescent staining of horizontal spinal sections showed angiogenesis in the (e) PBS (e1, e2), (f) sEV (f1, f2), and (g) NT3-sEV (g1, g2) groups. Enlarged images in e1, e2, f1, f2, and g1, g2 were from white dotted boxed regions in panels (e)–(g), respectively. (h) There was a significant increase of CD31 immunoreactivities in the sEV and NT3-sEV groups compared to the PBS group, more in the NT3-sEV group than the sEV group. Anti-5-HT immunofluorescent staining showed serotoninergic fibers in the (i) PBS (i1, i2), (j) sEV (j1, j2), and (k) NT3-sEV (k1, k2) groups. Enlarged images in i1, i2, j1, j2, and k1, k2 were from white dotted boxed regions in panels (i)–(k), respectively. Statistics revealed a significant increase of fiber densities in the NT3-sEV group, but not in the sEV group, compared to the PBS group (panel (l)). $^{*}P < 0.05$; $^{**}P < 0.01$; $^{***}P < 0.001$; $^{****}P < 0.0001$; one-way ANOVA multiple comparison and Tukey post hoc; 4 mice in each group.

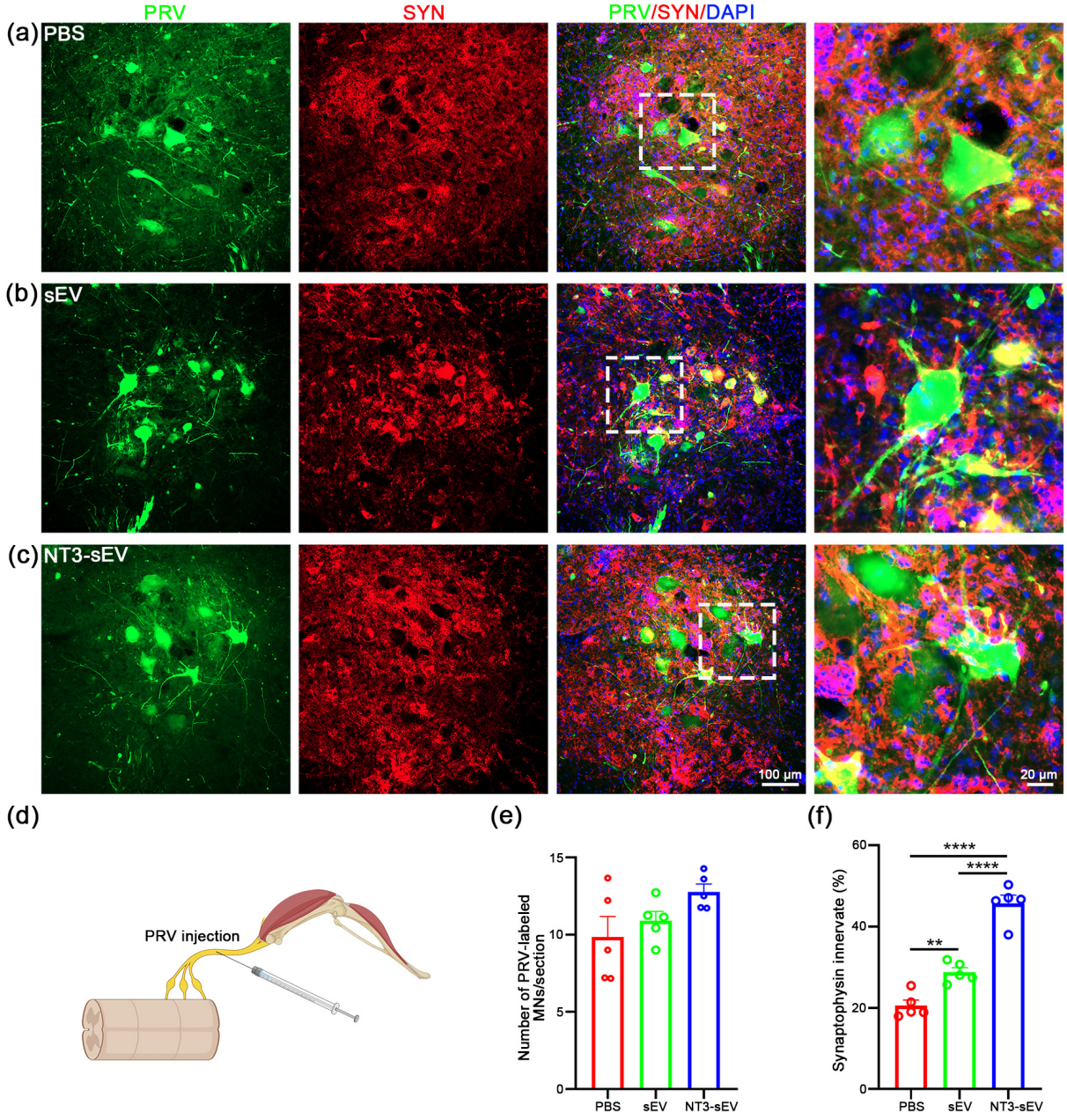

Figure 4 NT3-sEVs superiorly delay synaptic denervation of lumbar motoneurons after SCI over sEVs. (a)–(c) Presynaptic vesicles were studied by anti-synaptophysin (SYN, red) immunostaining in transverse spinal sections after 56 days post-SCI in three groups. Presynaptic vesicles on motoneurons were readily identified in the enlarged images (right panels). (d) PRV (green) retrograde tracing was used to label lumbar motoneurons. (e) The numbers of PRV-labelled lumbar motoneurons were comparable in three groups, whereas (f) the coverage of presynaptic vesicles on motoneurons was significantly increased in the sEV and NT3-sEV groups compared to the PBS group, with more in the NT3-sEV group than the sEV group. $^{**}P < 0.01$; $^{***}P < 0.001$; $^{****}P < 0.0001$; one-way ANOVA multiple comparison and Tukey post hoc; 5 mice in each group.

(neurons/section) 9.85 ± 2.96 in the PBS group, 10.91 ± 1.351 in the sEV group, and 12.77 ± 1.142 in the NT3-sEV group, showing an increasing trend in the NT3-sEV and sEV groups compared to the PBS group, though no significant differences were observed (Fig. 4(e)). We then quantified the innervation density of Synaptophysin surrounding individual motoneurons (soma and neurites) (Figs. 4(a)–4(c)) and found a significant increase in both the NT3-sEV group (45.72 ± 4.583) and the sEV group (28.78 ± 2.50) compared to the PBS group (20.57 ± 3.03), with a significantly greater increase in the NT3-sEV group than the sEV group (Fig. 4(f)). Thus, intranasal administration of NT3-sEVs and sEVs enhances synaptic plasticity and/or reduces synaptic loss on lumbar spinal motoneurons after SCI.

3.8 NT3-sEV and sEV administration alleviates glial response in the injured spinal cords

To further elucidate neuroinflammatory changes in the injured spinal cord, spinal tissues were collected on day 56 after SCI and glial response was analyzed using horizontal spinal sections by immunostaining. In the lesion border, anti-GFAP immunostaining showed reactive astrocytes with hypertrophied somas and processes surrounded the lesion in the PBS group, while reactive astrocytes

were reduced in the NT3-sEV and sEV groups (Figs. S5(a) and S5(c) in the ESM).

The density of reactive astrocytes was significantly higher in the PBS group (229.0 ± 19.76 cells/mm^2) compared to the sEV group (186.6 ± 14.84 cells/mm^2) and the NT3-sEV group (150.2 ± 24.89 cells/mm^2), which was significantly lower in the NT3-sEV group than the sEV group (Fig. S5(d) in the ESM).

Microglial response was studied by anti-Iba1 and -CD68 double immunofluorescent staining (Fig. S5(b) in the ESM). Around the lesion, Iba1-positive activated microglia were characterized by enlarged soma, amoeboid shape, and thickened and stubby processes. The density of Iba1-positive microglia was significantly higher in the PBS group (129.2 ± 10.06 cells/mm^2) than the sEV group (101.0 ± 13.84 cells/mm^2) and the NT3-sEV group (78.8 ± 10.18 cells/mm^2), with a lower density in the NT3-sEV than the sEV group (Fig. S5(e) in the ESM).

In addition, many Iba1-positive cells were positive for CD68 (a marker for pro-inflammatory type) in the PBS group, whereas the proportion of double-positive cells was lower in the NT3-sEV and sEV groups (Fig. S5(b) in the ESM). Statistical analysis showed a significant decrease in ratios (CD68$^+$Iba1$^+$ cells / Iba1$^+$ cells) in the sEV and NT3-sEV groups compared to the PBS group (Fig. S5(f) in the ESM). Thus, intranasal administration of sEVs and NT3-sEVs in the acute phase of SCI significantly reduces glial response identified in the chronic phase of SCI.

3.9 Administration of NT3-sEVs activates the NT3-TrkC signaling *in vivo* after SCI

It has been widely demonstrated that NT3 plays a critical role in promoting neuronal survival and axonal regeneration by binding TrkC receptor to activate downstream partners such as PLC, protein kinase C (PKC) and extracellular signal-regulated kinase (ERK) [47]. To investigate whether intranasal delivery of NT3-sEVs enhances the concentration of NT3 in injured spinal cords, intranasal administration of PBS, sEVs, and NT3-sEVs was performed once at 2 h following SCI. Spinal cord tissues including lesion sites were harvested on post-injury days 1, 3, and 5, and NT3 levels were quantified using ELISA. The results demonstrated that the NT3 concentration in the NT3-sEV group was significantly elevated compared to the PBS and sEV groups on days 1 and 3 post-injury; however, this difference was no longer statistically significant by day 5. Furthermore, on day 1 post-injury, NT3 levels in both the PBS and sEV groups exceeded those observed in the Sham group (Fig. S6 in the ESM). To further determine if intranasal administration of NT3-sEVs activated the NT3-TrkC signaling pathway *in vivo*, we collected spinal samples after 7 days of SCI for Western blots (Fig. 5(a)). As expected, the phosphorylation of TrkC, PLC, PKC and ERK was significantly upregulated in the NT3-sEV group compared to the sEV and PBS groups (Figs. 5(a)–5(e)). Interestingly, sEV administration also induced a subtle increase in PLC phosphorylation compared to the PBS group (Figs. 5(a) and 5(c)).

In addition, we evaluated the expression of growth associated protein 43 (GAP43), Synaptophysin and Map2 (Fig. 5(a)), which reflect axon growth abilities, synaptic plasticity and neuronal survival respectively. There was a significant increase of GAP43 protein in the NT3-sEV group compared to the sEV and PBS groups (Fig. 5(f)). Synaptophysin protein levels were significantly increased in both sEV and NT3-sEV groups compared to the PBS group (Fig. 5(g)). The upregulation of Map2 reached a significant level in the NT3-sEV group but not in the sEV group compared to the PBS group (Fig. 5(h)). Thus, intranasal administration of NT3-sEVs significantly enhances NT3-associated TrkC signaling and downstream PLCγ–PKC–ERK pathway activation *in vivo* after SCI (Fig. 5(i)), which is accompanied by improved neural repair compared with sEVs.

3.10 Intranasal administration of NT3-sEVs alters transcriptomic profile in lesioned spinal cords

In addition to NT3 protein, NT3-sEVs carry abundant nucleic acids, such as miRNAs from donor MSCs, which may modulate the transcriptomics in targeted cells. To verify this hypothesis, we collected spinal samples including lesioned segments at day 7 after SCI for RNA-seq. A large number of differently-expressed genes (DEGs) were identified among four groups (Sham, PBS, sEV, and NT3-sEV) (Fig. S7(a) in the ESM).

There were 1345 DEGs between the NT3-sEV group and the sEV group, including 1254 with upregulation and 100 with downregulation in the NT3-sEV group compared to the sEV group (Fig. 6(a)). Representative DEGs with clear functional relevance were selectively labeled in the volcano plot to highlight pathways associated with axon regeneration, synaptic plasticity, and neuroinflammatory regulation. These DEGs were subjected to GO analysis based on their predicted function in biological processes, showing that most enriched signaling pathways were related to synaptic signaling and transmission, synaptic vesicle transport, and synapse organization (17/25) among the top 25 enriched terms (Fig. 6(b)).

We further performed KEGG analysis and clustered top 25 signaling pathways from 1345 DEGs (Fig. 6(c)). Most of them were involved in neuronal and/or synaptic plasticity, such as neuroactive ligand-receptor interaction (top 1st), GABAergic synapse (top 2nd), glutamatergic synapse (top 4th), synaptic vesicle cycle (top 5th), calcium signaling pathway (top 7th), cAMP signaling (top 11th), dopaminergic synapse (top 14th), cholinergic synapse (top 18th), serotonergic synapse (top 24th), and long-term potentiation (Fig. 6(c)). Based on KEGG analysis, GESA analysis further showed a significant upregulation of the neuroactive ligand-receptor interaction (Fig. 6(d), nuclear export signal (NES) =1.705, FDR = 0.003), the synaptic vesicle cycle (Fig. 6(e); NES = 1.694, FDR = 0.003), and the neurotransmitter receptors and postsynaptic signal transmission (Fig. 6(f); NES = 1.95, FDR = 0.0001) in the NT3-sEV group compared to the sEV group. In addition, 354 DEGs were identified between the NT3-sEV and PBS groups, which were subjected to GSEA analysis showing a significant upregulation of neuroactive ligand-receptor interaction (Fig. S7(b) in the ESM, NES = 1.906, FDR = 0.000), synaptic vesicle cycle (Fig. S7(c) in the ESM, NES = 1.766, FDR = 0.003), neurotransmitter release cycle (Fig. S7(d) in the ESM, NES = 2.168, FDR = 0.000), Dopamine neurotransmitter release cycle (Fig. S7(e) in the ESM, NES = 1.983, FDR = 0.000), and Serotonin neurotransmitter release cycle (Fig. S7(f) in the ESM, NES = 1.978, FDR = 0.000) in the NT3-sEV group compared to the PBS group.

DEGs were further clustered into different profiles according to their expression changes across the four groups (PBS vs. sEV vs. NT3-sEV vs. sham) (Fig. 6(g)). One cluster of DEGs with a continuous upregulation were subjected to KEGG analysis, and top 25 pathways were involved in neuronal and synapse plasticity (e.g., Glutamatergic, GABAergic, Dopaminergic synapses), neurodegeneration diseases, metabolic pathways, oxidative

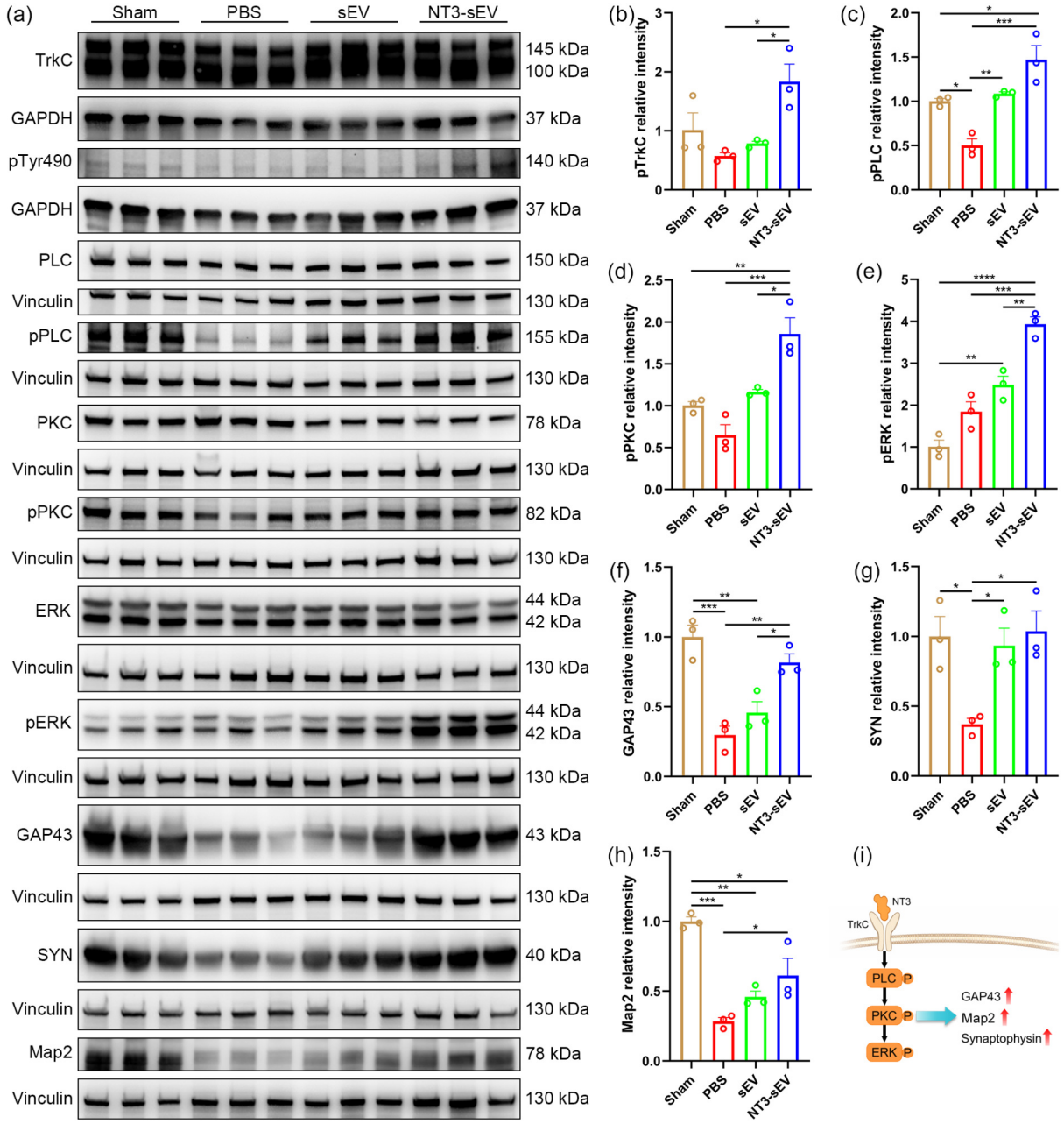

Figure 5 NT3-sEV administration activates the NT3/TrkC signaling pathway and enhances neuronal-related proteins *in vivo*. (a) At day 7 after SCI, spinal cord samples were subjected to Western blots using antibodies against TrkC, phosphorylated TrkC (pTyr490), PLC, phosphorylated PLC*γ* (pPLC*γ*), PKC, phosphorylated PKC (pPKC), ERK, phosphorylated ERK (pERK), GAP43, synaptophysin (SYN), and Map2. Antibodies against GAPDH and Vinculin were used for reference controls. Quantitative analysis showed a significant increase in phosphorylation levels of (b) TrkC (pTyr490/TrkC), (c) PLCγ (p-PLCγ/PLC), (d) PKC (pPKC/PKC), and (e) ERK (p-ERK/ERK) in the NT3-sEV group compared to the PBS and sEV groups. (f) The expression of GAP43 was significantly upregulated in the NT3-sEV group compared to the PBS and sEV groups. (g) Compared to the PBS group, upregulation of SYN was identified in both the NT3-sEV and sEV groups, whereas (h) upregulation of Map2 was only found in the NT3-sEV group. (i) Schematic diagram illustrating NT3-mediated activation of the TrkC–PLC*γ*–PKC–ERK signaling pathway, resulting in the upregulation of GAP43, Map2, and Synaptophysin. $^{*}P < 0.05$; $^{**}P < 0.01$; $^{***}P < 0.001$; one-way ANOVA.

phosphorylation, calcium signaling pathway, and neuroactive ligand-receptor interaction (Fig. 6(h)).

Key genes from these pathways—such as *Cacna1b, Fgf12, PrkcZ, Syn2, Fgf9, Grm1, Scn8a, Mapt (Tau), Trim9, Ryr2, Gria1, Nrxn1, Dlg4, Map2, Gabra1, Grbra2, Grin2d, Ndrg2, Rab3b, Pvalb,* and *Gap43* — showed the lowest expression in the PBS group and a stepwise increase across the sEV, NT3-sEV, and sham groups (Fig. 6(i)).

3.11 Intranasal administration of NT3-sEVs and sEVs induces proteomic alterations in injured spinal cords

To further elucidate the potential mechanisms underlying the therapeutic effects of NT3-sEVs and sEVs in SCI mice, injured spinal samples were collected on day 7 after SCI and subjected to proteomic analysis using a data-independent acquisition (DIA) strategy (Fig. 7(a)). A large number of differentially expressed proteins (DEPs) were identified through pairwise comparisons

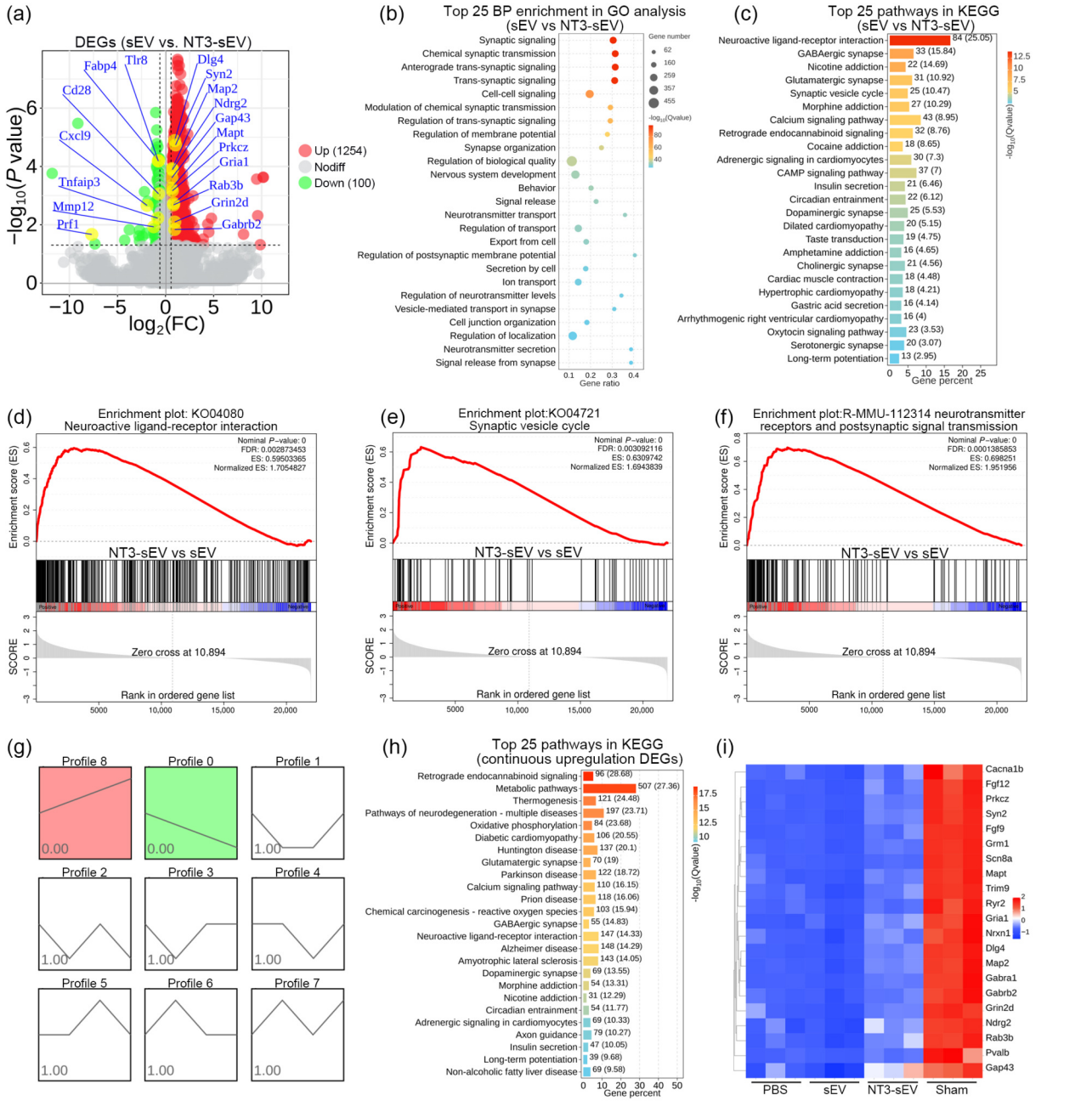

Figure 6 NT3-sEV administration induces transcriptomic alteration of injured spinal cords. (a) RNAseq of injured spinal cords identified 1254 upregulated DEGs (differently-expressed genes) and 100 downregulated DEGs in the NT3-sEV group compared to the sEV group ($|\log_2\text{Fold changes}| > 1.5$, $P < 0.05$) and representative DEGs were indicated. (b) GO analysis showed top 25 biological process-based enrichments and (c) KEGG analysis identified top 25 pathways from the DEGs between the NT3-sEV group and the sEV group. (d) GESA analysis uncovered a significant upregulation of the neuroactive ligand-receptor interaction, (e) the synaptic vesicle cycle, and (f) the neurotransmitter receptors and postsynaptic signal transmission in the NT3-sEV group compared to the sEV group. (g) DEGs were clustered into different profiles according to their expression changes across four groups (left to right in each profile: PBS, sEV, NT3-sEV, sham). (h) DEGs with a consistent upregulation across four groups were subjected to KEGG analysis showing top 25 pathways and the (i) representative DEGs were indicated in the heatmap.

among the four groups, and specifically, 332 DEPs (151 upregulation and 181 downregulation) were found in the NT3-sEV group compared to the sEV group (Fig. 7(b)).

DEPs were further clustered based on their changes from the PBS group to the sEV group to the NT3-sEV group and finally the sham group. We focused on the cluster (117 DEPs) with a consistent upregulation (Fig. 7(c)). KEGG pathway enrichment analysis revealed that these DEPs were clustered in many pathways highly related to synaptic plasticity and axonal growth, such as dopaminergic synapses, axon guidance, cholinergic synapses, glutamatergic synapse, citrate cycle (TCA cycle), serotonergic synapses, and cAMP signaling (Fig. 7(d)). Cellular component-based GO analysis revealed that top 25 enrichments were mainly implicated in synapses, neuron projection, axon, dendrite, neuron to neuron synapse, neuronal cell body, and myelin sheath (Fig. 7(e)), all of which are crucial for the maintenance of neuronal structure and function. Among these DEPs with a consistent upregulation (PBS vs. sEV vs. NT3-sEV vs. sham), many of them

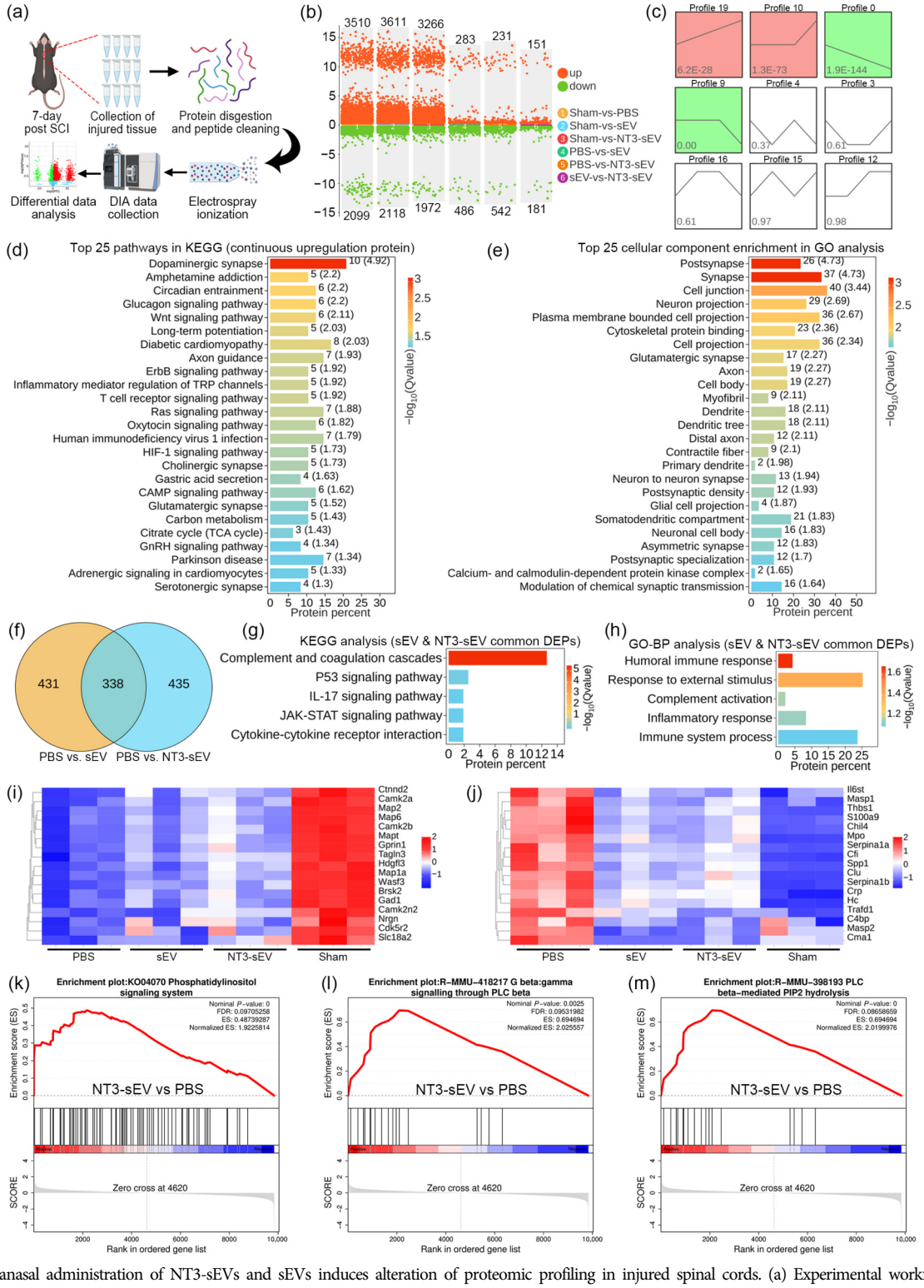

Figure 7 Intranasal administration of NT3-sEVs and sEVs induces alteration of proteomic profiling in injured spinal cords. (a) Experimental workflow illustrates proteomic analysis from cord samples at day 7 after SCI using a DIA-based strategy. (b) DEPs were shown in the volcano plots among the four groups ($|\log_2 \text{Fold changes}| > 1.2$, $P < 0.05$), and (c) DEPs were clustered into different profiles according to their expression changes in four groups (left to right: PBS vs. sEV vs. NT3-sEV vs. sham). (d) DEPs with a consistent upregulation across four groups (profile 19 in pnael (c)) were subjected to KEGG analysis showing top 25 pathways and (e) underwent GO analysis identifying top 20 cellular component-based enrichments. (f) 338 common DEPs were identified in the sEV and NT3-sEV groups compared to the PBS group, and (g) they were clustered into the pathways using KEGG analysis and (h) biological process-based enrichments using GO analysis. (i) The heatmaps showed the representative DEPs with a consistent upregulation across four groups and (j) the representative DEPs expressing with highest levels in the PBS group, middle levels in the sEV and NT3-sEV groups, and low levels in the sham group. GSEA enrichment analysis of DEPs (the NT3-sEV group vs. the PBS group) revealed a significant upregulation of (k) the phosphatidylinositol signaling system, (l) G beta: gamma signaling through PLC beta and (m) PLC beta-mediated PIP2 hydrolysis in the NT3-sEV group compared to the PBS group.

regulated neuronal cytoskeleton organization (e.g., Map2, Map6, Map1a, Tau (Mapt), Tagln3 and Wasf3), neuronal outgrowth (e.g., Ctnnd2, Gprin1, Hdgfl3, Brsk2, Cdk5r2), and neural/synaptic plasticity (e.g., Camk2a, Camk2b, Camk2n2, Gad1, Nrgn, Slc18a2) (Fig. 7(i)). The findings demonstrate that SCI results in the downregulation of neuron-associated proteins (as seen in the PBS group) and the administration of sEVs and NT3-sEVs effectively reverses the SCI-induced changes, with better effect in the NT3-sEV group compared to the sEV group.

It has been well demonstrated that MSCs play important roles in regulating neuroinflammation and immunomodulation [48]. We hypothesized that both sEVs and NT3-sEVs would retain the immunomodulatory functions of MSCs. In the proteomic analysis, there were 338 common DEPs in the sEV and NT3-sEV groups compared to the PBS group (Fig. 7(f)). KEGG analysis showed that these DEPs were clustered in the signaling pathways including complement and coagulation, P53 signaling pathway, IL-17 signaling pathway, JAK-Stat signaling pathway, and cytokine-cytokine receptor interaction (Fig. 7(g)). Biological process-based GO analysis also indicated that these DEPs were enriched in inflammation and immune processes (Fig. 7(h)). A great number of pro-inflammatory or inflammation-associated proteins were identified to upregulate in the PBS group and to downregulate in both the sEV and NT3-sEV groups, including Il6st, Masp1, Thbs1, S100a9, Chil4, Mpo, Serpina1a, Cfi, Spp1, Clu, Serpina1b, Crp, Hc, Tradfd1, C4bp, Masp2, and Cma1 (Fig. 7(j)).

In the Western blots analysis, we showed that the administration of NT3-sEVs, but not of sEVs, effectively activated the NT3-TrkC signaling pathway *in vivo*. In the proteomic analysis, we further performed GSEA analysis of DEPs between the NT3-sEV group and the PBS group. There was a significant upregulation of Phosphatidylinositol signaling system (Fig. 7(k); NES = 1.92, FDR = 0.097), G$\beta\gamma$ signaling through PLCβ (Fig. 7(l); NES = 2.03, FDR = 0.095) and PLCγ-mediated phosphatidylinositol 4,5-bisphosphate (PIP2) hydrolysis (Fig. 7(m); NES = 2.02, FDR = 0.086) in the NT3-sEV group compared to the PBS group, and all these signaling pathways are the important downstream partners of the NT3-TrkC signaling.

3.12 Enriched miRNAs in NT3-sEVs and sEVs potentially regulate gene expression in injured spinal cords

Abundant miRNAs in sEVs are key post-transcriptional regulators in targeted cells by inhibiting translation and promoting mRNA degeneration [49]. Using small RNA-seq, we identified 65 and 53 miRNAs with high abundance (TPM > 1000) in sEVs and NT3-sEVs, respectively (Fig. 8(a)), among which there were 32 common miRNAs in sEVs and NT3-sEVs (Fig. 8(b)). KEGG analysis of these common miRNAs showed that they were enriched in many signaling pathways related to neuronal death and neuroinflammation such as FoxO signaling, MAPK signaling, ErbB signaling, mTOR signaling, Ras signaling, TGF-β signaling, Sphingolipid signaling, P53 signaling, TNF signaling, and AMPK signaling (Fig. 8(c)). These common miRNAs were subjected to an integrative analysis of their interactions with potential mRNAs and the functional interaction network was visualized using a Sankey diagram. Using this method, we found that these miRNAs crossly interacted with multiple mRNAs, which were mainly involved in promoting neuronal death (e.g., *Bcl2*, *JNK2*, *Nprl3*, *Caspase3*, *Capse8*, *Caspase9*), enhancing neuroinflammation and immune responses (e.g., *NF-κB*, *TNFα*, *TGFß*, *mTOR*, *Kras*, *VEGFc*, *Akt*, *PI3K*, *IL1*, *IL6*, *IL8*, *Myd88*), and inhibiting axonal regeneration (e.g., *PTEN*) (Fig. 8(d)). The result suggests that abundant miRNAs in sEVs and NT3-sEVs play common roles in promoting neuronal survival and alleviating neuroinflammation through inhibiting targeted gene expression. To confirm this, we compared the protein expression levels of these miRNA-targeted genes in our proteomic studies of spinal cords samples in the PBS, sEV and NT3-sEV groups. Average expression levels of proteins were normalized to those in the PBS group, showing downregulation of proteins related to neuronal death (Bcl2, Caspase3, Caspase8, Caspase 9, Nplr3) and neuroinflammation (nuclear factor kappa B (NF-κB), tumor necrosis factor alpha (TNFα), transforming growth factor beta (TGFβ), interleukin 1 (IL1), IL6, IL8, Myd88) in the sEV and NT3-sEV groups (Fig. S8 in the ESM).

Intranasal administration of NT3-sEVs induced remarkable alterations of transcriptomic and proteomic profiles in injured spinal cords compared to that of sEVs, suggesting that NT3-sEVs may carry additional bioactive components beyond NT3 protein. In support of this hypothesis, we identified 46 differently-expressed miRNAs ($|\log_2$Fold change$| > 2.0$, $P < 0.05$), including 17 miRNAs with upregulation and 29 miRNAs with downregulation in NT3-sEVs compared to sEVs (Figs. 8(e)–8(g)). GO analysis showed that top 20 biological process-based enrichments of these altered miRNAs were involved in neuronal apoptosis and death, ion transport on membrane, and action potential (Fig. 8(h)). We further performed KEGG analysis of these miRNAs and found that the top 20 enriched pathways included cytokine-cytokine receptor interaction, neurotrophin signaling, neuroactive ligand-receptor interaction, serotonergic synapse, nod-like receptor signaling, Sphingolipid signaling, and inflammatory mediator regulation (Fig. 8(i)). These results suggest that altered miRNAs in NT3-sEVs may impose different effects on neuroprotection, neural repair, and the regulation of inflammation and immune responses compared to sEVs.

4 Discussion

Promoting neural repair and functional recovery after SCI necessitates the development of a combined therapeutic strategy, as traumatic insult typically triggers a complex pathological process characterized by intertwined neuronal damage and neuroinflammatory cascades, particularly during the acute phase [50]. By leveraging the beneficial roles of MSCs-derived sEVs and NT3 in neural repair, we developed NT3-loaded sEVs (NT3-sEVs) and demonstrated that their intranasal delivery serves as an effective therapeutic strategy for acute SCI. We gained high-quality, relatively stable sEVs and NT3-sEVs using immortalized iPSC-derived MSCs. Importantly, our previous work has demonstrated that neurotrophin-loaded MSC-sEVs (e.g., BDNF-sEVs) retain structural integrity and biological activity even after 3- or 5-months of storage at −80 °C, and given the identical production and storage workflow applied in the present study, this provides methodological support for the stability of NT3-MSC-sEVs used here. These cells possess significant advantages, including immunosuppressive and low immunogenic properties [51], no signs of senescence from passages 5 to 18, and only minimal senescence observed at passage 50 [43]. This therapeutic approach not only overcomes the challenges associated with MSC transplantation for treating acute SCI [52] but also addresses the difficulty of exogenous NT3 crossing the blood–brain barrier (BBB) and its rapid *in vivo*

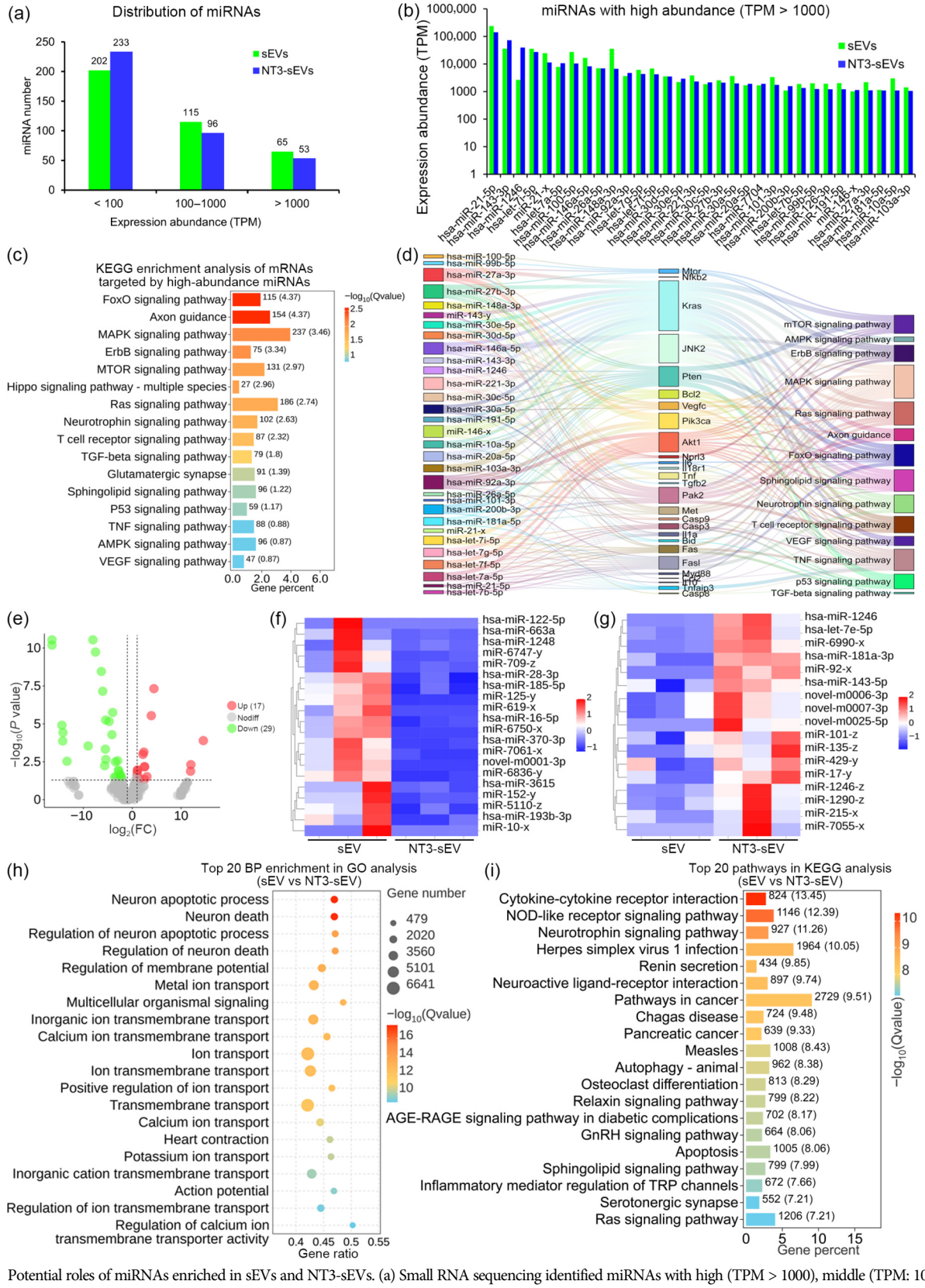

Figure 8 Potential roles of miRNAs enriched in sEVs and NT3-sEVs. (a) Small RNA sequencing identified miRNAs with high (TPM > 1000), middle (TPM: 100–1000), and low (TPM < 100) abundance in sEVs and NT3-sEVs. (b) There were 32 common miRNAs with high abundance in sEVs and NT3-sEVs and (c) KEGG analysis of their targeted genes showed enriched signaling pathways. (d) The Sankey diagram displayed the miRNA-mRNA interaction network and the related signaling pathways (left panel: miRNAs; middle panel: targeted genes; right panels: GO enrichments; line thickness: interaction strength). (e) There were 46 differently-expressed miRNAs in NT3-sEVs compared to sEVs (|Log_2Fold changes| > 2.0, P < 0.05), including (f) 29 miRNAs with downregulation and (g) 17 miRNAs with upregulation. GO analysis showed top 20 biological process-based enrichments (in panel (d)) and KEGG analysis identified top 20 pathways (in panel (e)).

degradation [53]. Moreover, intranasal administration can be flexibly adjusted in terms of timing and dosage, while effectively minimizing the impact on peripheral organs. Our study provides strong evidence that NT3-sEVs exert significantly better effects than sEVs alone in treating acute SCI, attributed to the loaded NT3 protein and modifications to other bioactive components of NT3-sEVs compared to sEVs.

NT3 plays a critical role in neural development and promotes neural repair through its receptors (e.g., TrkC) expressing in most neurons (e.g., spinal motoneurons) and axons of long projecting neurons [39]. Enhancing NT3 protein levels at the lesion site has been proposed as an important strategy in treating SCI, including designing delivery systems using chitosan and hydrogels or transfecting NT3-overexpressed lentivirus *in vivo* [54–56]. Our study demonstrates that MSCs-derived sEVs represent another viable option for delivering NT3. Purified sEVs from NT3-overexpressing MSCs contained abundant NT3 proteins, as verified by Western blots and ELISA, and NT3 loading did not remarkably alter the physical characteristics of NT3-sEVs such as nanoparticle size and homogeneity. In cultured neurons, administration of NT3-sEVs more efficiently promoted neurite outgrowth and branching compared to sEVs, suggesting the beneficial contribution of NT3 from NT3-sEVs. In addition, NT3 overexpression may enhance the production of sEVs from cultured MSCs, as evidenced by the higher density of NT3-sEVs harvested compared to sEVs from comparable volumes of MSC culture.

Increasing evidence supports intranasal administration as a reasonable route for CNS-targeted drugs via the terminus of olfactory nerves or intercellular junctions of olfactory bulbs [34, 57]. Although sEVs can enter the CNS through other routes such as intravenous injection, intranasal administration effectively enhances sEV distribution in the CNS and limits their impact on peripheral organs [58]. Consistent with this, our study showed that mCherry-sEVs rapidly reached the lesion surroundings and other brain regions within 24 h of intranasal administration and were up taken by most neurons and some glial cells in the SCI mice. Our recent work also demonstrated that intranasally-delivered sEVs readily reached the CNS in non-human primates [59], suggesting that this delivery method is applicable to humans as well.

Our *in vivo* studies demonstrate that intranasal administration of both NT3-sEVs and sEVs represents effective therapeutic options for acute SCI treatment, with NT3-sEVs exhibiting significantly greater efficacy than sEVs. Notably, the dosing regimen used in the present study was based on our previous dose-gradient analysis of intranasally delivered MSC-sEVs in a CNS injury model, in which a higher dose (3×10^9 particles per mouse) produced significantly superior functional recovery compared with a lower dose (3×10^8 particles), while remaining well tolerated. Typical pathological features of SCI include neuronal death, lesion cavity formation, fiber disruption, and glial responses, all of which were significantly alleviated in injured spinal cords following 7-day intranasal administration of both sEVs and NT3-sEVs during the acute phase. Administration facilitated angiogenesis and axon regeneration (e.g., serotoninergic fibers), with superior outcomes observed from NT3-sEVs compared to sEVs. SCI at thoracic segments interrupted descending inputs to lumbar spinal motoneurons, which directly drive hind limb movement, and synaptic denervation on lumbar motoneurons account for hind limb paralysis. Our results showed that the coverage of presynaptic vesicles was significantly increased in the sEV and NT3-sEV groups compared to the PBS group, with better efficacy from NT3-sEVs over sEVs. These morphological changes correlated well with the functional improvements observed in behavioral tests and EMG recordings. Thus, NT3-sEVs share the common beneficial roles of sEVs in neural repair by promoting neural and synaptic plasticity, and inhibiting neuroinflammation, consistent with findings in ischemia stroke and amyotrophic lateral sclerosis mouse models [21, 60].

The superior outcomes induced by intranasal administration further indicate that NT3-sEVs exert the combined therapeutic effects of sEVs and NT3. Firstly, intranasal administration of NT3-sEVs, but not sEVs, effectively activated the NT3-TrkC signaling pathway *in vivo* as identified by a significant upregulation of phosphorylated key downstream components including TrkC, PLC, PKC, and ERK, as well as supported by proteomic studies of spinal cord samples, in which GSEA enrichment analysis of DEPs between the NT3-sEV and PBS groups showed the upregulation of phosphatidylinositol signaling system, G$\beta\gamma$ signaling through PLCβ and PLCγ-mediated PIP2 hydrolysis, belonging to downstream partners of the NT3-TrkC signaling pathway [47]. Western blot analysis showed increased levels of GAP43, Synaptophysin, and Map2 proteins in the NT3-sEV group, indicating enhanced neuronal regeneration (indicated by GAP43), synaptic plasticity (indicated by Synaptophysin), and neuronal survival (indicated by Map2). These results confirmed that sEVs serve as the reliable carriers for transporting NT3 to the lesion site after SCI.

The abundant components contained in sEVs determine their multi-molecular targeting effects *in vivo*, similar to transplanted MSCs. Using transcriptomic and proteomic studies, we identified a large number of DEGs and DEPs in the injured spinal cord following intranasal administration of sEVs and NT3-sEVs compared to PBS. DEGs and DEPs between the NT3-sEV and the sEV groups were clustered into many signaling pathways related to neural and synaptic plasticity and neuronal regeneration, and many neuron- and regeneration-associated DEGs and DEPs showed a continuous upregulation across four groups (PBS vs. sEV vs. NT3-sEV vs. sham), such as Tau and Map2 identified in both DEGs and DEPs. These results suggest that intranasal administration of NT3-sEVs more effectively promotes neural repair than that of sEVs. We also identified many common DEPs in the NT3-sEV and sEV groups, which were mainly clustered into the signaling pathways related to neuroinflammation and immune modulation. Many pro-neuroinflammatory DEPs similarly downregulated in the NT3-sEV and sEV groups. Based on the changes of transcriptomic and proteomic profiles, we predict that many other components in NT3-sEVs differ from those in sEVs beyond the loaded NT3 protein, potentially due to the impact of NT3 overexpression in cultured MSCs.

NT3-sEVs retain the anti-inflammatory and neuroprotective properties inherent to sEVs. Small RNA sequencing revealed numerous abundant miRNAs shared between sEVs and NT3-sEVs, predicted to suppress proteins involved in neuroinflammation (e.g., TNFα, NF-κB, TGFβ, IL1, IL6, IL8, Myd88) and neuronal apoptosis (e.g., Bcl2, Caspase3, Caspase8, Caspase9, NLRP3). This prediction was supported by integrated analyses of miRNA-targeted mRNA signaling networks and confirmed by proteomic assessments of spinal cord tissues from sEV- and NT3-sEV-treated groups. Additionally, several miRNAs were differentially expressed specifically in NT3-sEVs, suggesting that components beyond NT3 protein contribute to the enhanced therapeutic efficacy observed with NT3-sEV administration.

5 Conclusions

In this study, we developed a novel and effective strategy for treating acute SCI through the intranasal administration of NT3-sEVs. This therapeutic approach promotes neural repair and functional improvement by activating the NT3-TrkC signaling pathway and modulating the transcriptomic and proteomic profiles in the injured spinal cord.

Electronic Supplementary Material: Supplementary material (Figs. S1–S8) is available in the online version of this article at https://doi.org/10.26599/NR.2026.94908424.

Data availability

All data needed to support the conclusions in the paper are presented in the manuscript and/or the Electronic Supplementary Material. Additional data related to this paper may be requested from the corresponding author upon request.

Acknowledgments

We wish to thank M. Z. W., J. W. Q., and Y. Q. L. for technical assistance. We also thank the Animal Magnetic Resonance Research Center at the First Affiliated Hospital of Jinan University for providing the essential equipment used in this study. This work was supported by the following grants: the National Key R&D Program of China (No. 2022YFA1104900, Q.-L. F. & L. B. Z.), Guangzhou Key Projects of Brain Science and Brain-Like Intelligence Technology (No. 20200730009, L. B. Z.; No. 202206060003, L. B. Z. & Q.-L. F.), and Guangdong grant "Key technologies for treatment of brain disorders" (No. 2018B030332001, L. B. Z.).

Declaration of competing interest

All the contributing authors report no conflict of interests in this work.

Author contribution statement

L. B. Z. conceived and designed the experiments; F. X. L. performed the experiments and validated the results; F. X. L., Z. H. H. and J. R. Z. worked in animal studies; F. X. L. and J. R. Z. developed the methodology and carried out the investigation; Z. C. W. and X.-H. D. prepared MSCs and sEVs; H. D. W., W. X. P., J. L., and Y. L. curated the data; L. B. Z., Q.-L. F., and K.-F. S. supervised the project; F. X. L. drafted the original manuscript; L. B. Z. edited the manuscript; L. B. Z. and Q.-L. F. revised the final version. All authors have read and approved the final manuscript.

Informed consent

Not applicable.

Ethics statement

All experimental procedures were conducted in accordance with the National Institutes of Health (NIH) Guide for the Care and Use of Laboratory Animals and were approved by the Animal Ethics Committee of Jinan University (Approval No.: IACUC-20220407-01).

Use of AI statement

AI-assisted technologies were used only for language polishing and grammar checking; all scientific content, interpretation, and conclusions were authored and verified by the authors.

References

[1] Hu, X.; Xu, W.; Ren, Y. L.; Wang, Z. J.; He, X. L.; Huang, R. Z.; Ma, B.; Zhao, J. W.; Zhu, R. R.; Cheng, L. M. Spinal cord injury: Molecular mechanisms and therapeutic interventions. *Signal Transduct. Target. Ther.* **2023**, *8*, 245.

[2] Anjum, A.; Yazid, M. D.; Fauzi Daud, M.; Idris, J.; Ng, A. M. H.; Selvi Naicker, A.; Ismail, O. H. R.; Athi Kumar, R. K.; Lokanathan, Y. Spinal cord injury: Pathophysiology, multimolecular interactions, and underlying recovery mechanisms. *Int. J. Mol. Sci.* **2020**, *21*, 7533.

[3] Lemon, R. N. Descending pathways in motor control. *Annu. Rev. Neurosci.* **2008**, *31*, 195–218.

[4] Petersen, J. A.; Wilm, B. J.; von Meyenburg, J.; Schubert, M.; Seifert, B.; Najafi, Y.; Dietz, V.; Kollias, S. Chronic cervical spinal cord injury: DTI correlates with clinical and electrophysiological measures. *J. Neurotrauma* **2012**, *29*, 1556–1566.

[5] Angeli, C. A.; Edgerton, V. R.; Gerasimenko, Y. P.; Harkema, S. J. Altering spinal cord excitability enables voluntary movements after chronic complete paralysis in humans. *Brain* **2014**, *137*, 1394–1409.

[6] Assinck, P.; Duncan, G. J.; Hilton, B. J.; Plemel, J. R.; Tetzlaff, W. Cell transplantation therapy for spinal cord injury. *Nat. Neurosci.* **2017**, *20*, 637–647.

[7] Galipeau, J.; Sensébé, L. Mesenchymal stromal cells: Clinical challenges and therapeutic opportunities. *Cell Stem Cell* **2018**, *22*, 824–833.

[8] Honmou, O.; Houkin, K.; Matsunaga, T.; Niitsu, Y.; Ishiai, S.; Onodera, R.; Waxman, S. G.; Kocsis, J. D. Intravenous administration of auto serum-expanded autologous mesenchymal stem cells in stroke. *Brain* **2011**, *134*, 1790–1807.

[9] Lou, G. H.; Chen, Z.; Zheng, M.; Liu, Y. N. Mesenchymal stem cell-derived exosomes as a new therapeutic strategy for liver diseases. *Exp. Mol. Med.* **2017**, *49*, e346.

[10] van Niel, G.; D'Angelo, G.; Raposo, G. Shedding light on the cell biology of extracellular vesicles. *Nat. Rev. Mol. Cell Biol.* **2018**, *19*, 213–228.

[11] Colombo, M.; Raposo, G.; Théry, C. Biogenesis, secretion, and intercellular interactions of exosomes and other extracellular vesicles. *Annu. Rev. Cell Dev. Biol.* **2014**, *30*, 255–289.

[12] Kalluri, R.; LeBleu, V. S. The biology, function, and biomedical applications of exosomes. *Science* **2020**, *367*, eaau6977.

[13] Park, J. E.; Tan, H. S.; Datta, A.; Lai, R. C.; Zhang, H. M.; Meng, W.; Lim, S. K.; Sze, S. K. Hypoxic tumor cell modulates its microenvironment to enhance angiogenic and metastatic potential by secretion of proteins and exosomes. *Mol. Cell. Proteomics* **2010**, *9*, 1085–1099.

[14] Kowal, J.; Arras, G.; Colombo, M.; Jouve, M.; Morath, J. P.; Primdal-Bengtson, B.; Dingli, F.; Loew, D.; Tkach, M.; Théry, C. Proteomic comparison defines novel markers to characterize heterogeneous populations of extracellular vesicle subtypes. *Proc. Natl. Acad. Sci. USA* **2016**, *113*, E968–E977.

[15] Zhang, Z. G.; Buller, B.; Chopp, M. Exosomes-beyond stem cells for restorative therapy in stroke and neurological injury. *Nat. Rev. Neurol.* **2019**, *15*, 193–203.

[16] Joo, H. S.; Suh, J. H.; Lee, H. J.; Bang, E. S.; Lee, J. M. Current knowledge and future perspectives on mesenchymal stem cell-derived exosomes as a new therapeutic agent. *Int. J. Mol. Sci.* **2020**, *21*, 727.

[17] Chen, C. C.; Liu, L. N.; Ma, F. X.; Wong, C. W.; Guo, X. E.; Chacko, J. V.; Farhoodi, H. P.; Zhang, S. X.; Zimak, J.; Ségaliny, A. et al. Elucidation of exosome migration across the blood-brain barrier model *in vitro*. *Cell. Mol. Bioeng.* **2016**, *9*, 509–529.

[18] Lo Cicero, A.; Stahl, P. D.; Raposo, G. Extracellular vesicles shuffling intercellular messages: For good or for bad. *Curr. Opin. Cell Biol.* **2015**, *35*, 69–77.
[19] Yáñez-Mó, M.; Siljander, P. R. M.; Andreu, Z.; Zavec, A. B.; Borràs, F. E.; Buzas, E. I.; Buzas, K.; Casal, E.; Cappello, F.; Carvalho, J. et al. Biological properties of extracellular vesicles and their physiological functions. *J. Extracell. Vesicles* **2015**, *4*, 27066.
[20] Yeo, R. W. Y.; Lai, R. C.; Zhang, B.; Tan, S. S.; Yin, Y. J.; Teh, B. J.; Lim, S. K. Mesenchymal stem cell: An efficient mass producer of exosomes for drug delivery. *Adv. Drug Deliv. Rev.* **2013**, *65*, 336–341.
[21] Zhou, X.; Deng, X. H.; Liu, M. F.; He, M. T.; Long, W. H.; Xu, Z. B.; Zhang, K.; Liu, T.; So, K. F.; Fu, Q. L. et al. Intranasal delivery of BDNF-loaded small extracellular vesicles for cerebral ischemia therapy. *J. Control. Release* **2023**, *357*, 1–19.
[22] Alvarez-Erviti, L.; Seow, Y.; Yin, H. F.; Betts, C.; Lakhal, S.; Wood, M. J. A. Delivery of siRNA to the mouse brain by systemic injection of targeted exosomes. *Nat. Biotechnol.* **2011**, *29*, 341–345.
[23] Didiot, M. C.; Hall, L. M.; Coles, A. H.; Haraszti, R. A.; Godinho, B. M.; Chase, K.; Sapp, E.; Ly, S.; Alterman, J. F.; Hassler, M. R. et al. Exosome-mediated delivery of hydrophobically modified siRNA for huntingtin mRNA silencing. *Mol. Ther.* **2016**, *24*, 1836–1847.
[24] Qu, M. K.; Lin, Q.; Huang, L. Y.; Fu, Y.; Wang, L. Y.; He, S. S.; Fu, Y.; Yang, S. Y.; Zhang, Z. R.; Zhang, L. et al. Dopamine-loaded blood exosomes targeted to brain for better treatment of Parkinson's disease. *J. Control. Release* **2018**, *287*, 156–166.
[25] Zhuang, X. Y.; Xiang, X. Y.; Grizzle, W.; Sun, D. M.; Zhang, S. Q.; Axtell, R. C.; Ju, S. W.; Mu, J. Y.; Zhang, L. F.; Steinman, L. et al. Treatment of brain inflammatory diseases by delivering exosome encapsulated anti-inflammatory drugs from the nasal region to the brain. *Mol. Ther.* **2011**, *19*, 1769–1779.
[26] Haney, M. J.; Klyachko, N. L.; Zhao, Y. L.; Gupta, R.; Plotnikova, E. G.; He, Z. J.; Patel, T.; Piroyan, A.; Sokolsky, M.; Kabanov, A. V. et al. Exosomes as drug delivery vehicles for Parkinson's disease therapy. *J. Control. Release* **2015**, *207*, 18–30.
[27] Marote, A.; Teixeira, F. G.; Mendes-Pinheiro, B.; Salgado, A. J. MSCs-derived exosomes: Cell-secreted nanovesicles with regenerative potential. *Front Pharmacol* **2016**, *7*, 231.
[28] Perets, N.; Hertz, S.; London, M.; Offen, D. Intranasal administration of exosomes derived from mesenchymal stem cells ameliorates autistic-like behaviors of BTBR mice. *Mol. Autism.* **2018**, *9*, 57.
[29] Xin, H. Q.; Katakowski, M.; Wang, F. J.; Qian, J. Y., Liu, X. S.; Ali, M. M.; Buller, B.; Zhang, Z. G.; Chopp, M. MicroRNA-17-92 cluster in exosomes enhance neuroplasticity and functional recovery after stroke in rats. *Stroke* **2017**, *48*, 747–753.
[30] Williams, A. M.; Dennahy, I. S.; Bhatti, U. F.; Halaweish, I.; Xiong, Y.; Chang, P. P.; Nikolian, V. C.; Chtraklin, K.; Brown, J.; Zhang, Y. L. et al. Mesenchymal stem cell-derived exosomes provide neuroprotection and improve long-term neurologic outcomes in a swine model of traumatic brain injury and hemorrhagic shock. *J. Neurotrauma* **2019**, *36*, 54–60.
[31] Ni, H. Q.; Yang, S.; Siaw-Debrah, F.; Hu, J. N.; Wu, K.; He, Z. B.; Yang, J. J.; Pan, S. S.; Lin, X.; Ye, H. T. et al. Exosomes derived from bone mesenchymal stem cells ameliorate early inflammatory responses following traumatic brain injury. *Front. Neurosci.* **2019**, *13*, 14.
[32] Reza-Zaldivar, E. E.; Hernández-Sapiéns, M. A.; Minjarez, B.; Gutiérrez-Mercado, Y. K.; Márquez-Aguirre, A. L.; Canales-Aguirre, A. A. Potential effects of MSC-derived exosomes in neuroplasticity in Alzheimer's disease. *Front. Cell Neurosci.* **2018**, *12*, 317.
[33] Guo, S. W.; Perets, N.; Betzer, O.; Ben-Shaul, S.; Sheinin, A.; Michaelevski, I.; Popovtzer, R.; Offen, D.; Levenberg, S. Intranasal delivery of mesenchymal stem cell derived exosomes loaded with phosphatase and tensin homolog siRNA repairs complete spinal cord injury. *ACS Nano* **2019**, *13*, 10015–10028.
[34] Herman, S.; Fishel, I.; Offen, D. Intranasal delivery of mesenchymal stem cells-derived extracellular vesicles for the treatment of neurological diseases. *Stem Cells* **2021**, *39*, 1589–1600.
[35] Born, J.; Lange, T.; Kern, W.; McGregor, G. P.; Bickel, U.; Fehm, H. L. Sniffing neuropeptides: A transnasal approach to the human brain. *Nat. Neurosci.* **2002**, *5*, 514–516.
[36] Ruitenberg, M. J.; Levison, D. B.; Lee, S. V.; Verhaagen, J.; Harvey, A. R.; Plant, G. W. NT-3 expression from engineered olfactory ensheathing glia promotes spinal sparing and regeneration. *Brain* **2005**, *128*, 839–853.
[37] Zhou, L. J.; Baumgartner, B. J.; Hill-Felberg, S. J.; McGowen, L. R.; Shine, H. D. Neurotrophin-3 expressed *in situ* induces axonal plasticity in the adult injured spinal cord. *J. Neurosci.* **2003**, *23*, 1424–1431.
[38] Grill, R.; Murai, K.; Blesch, A.; Gage, F. H.; Tuszynski, M. H. Cellular delivery of neurotrophin-3 promotes corticospinal axonal growth and partial functional recovery after spinal cord injury. *J. Neurosci.* **1997**, *17*, 5560–5572.
[39] Schnell, L.; Schneider, R.; Kolbeck, R.; Barde, Y. A.; Schwab, M. E. Neurotrophin-3 enhances sprouting of corticospinal tract during development and after adult spinal cord lesion. *Nature* **1994**, *367*, 170–173.
[40] Duricki, D. A.; Hutson, T. H.; Kathe, C.; Soleman, S.; Gonzalez-Carter, D.; Petruska, J. C.; Shine, H. D.; Chen, Q.; Wood, T. C.; Bernanos, M. et al. Delayed intramuscular human neurotrophin-3 improves recovery in adult and elderly rats after stroke. *Brain* **2016**, *139*, 259–275.
[41] Skaper, S. D. Neurotrophic factors: An overview. In *Neurotrophic Factors: Methods and Protocols*. Skaper, S. D., Ed.; Springer: New York, 2017; pp 1–17.
[42] Zhang, Y. P.; Burke, D. A.; Shields, L. B. E.; Chekmenev, S. Y.; Dincman, T.; Zhang, Y. J.; Zheng, Y. Y.; Smith, R. R.; Benton, R. L.; DeVries, W. H. et al. Spinal cord contusion based on precise vertebral stabilization and tissue displacement measured by combined assessment to discriminate small functional differences. *J. Neurotrauma* **2008**, *25*, 1227–1240.
[43] Gao, W. X.; Sun, Y. Q.; Shi, J. B.; Li, C. L.; Fang, S. B.; Wang, D.; Deng, X. Q.; Wen, W. P.; Fu, Q. L. Effects of mesenchymal stem cells from human induced pluripotent stem cells on differentiation, maturation, and function of dendritic cells. *Stem. Cell Res. Ther.* **2017**, *8*, 48.
[44] Fang, S. B.; Zhang, H. Y.; Wang, C.; He, B. X.; Liu, X. Q.; Meng, X. C.; Peng, Y. Q.; Xu, Z. B.; Fan, X. L.; Wu, Z. J. et al. Small extracellular vesicles derived from human mesenchymal stromal cells prevent group 2 innate lymphoid cell-dominant allergic airway inflammation through delivery of miR-146a-5p. *J. Extracell. Vesicles* **2020**, *9*, 1723260.
[45] Husch, A.; Van Patten, G. N.; Hong, D. N.; Scaperotti, M. M.; Cramer, N.; Harris-Warrick, R. M. Spinal cord injury induces serotonin supersensitivity without increasing intrinsic excitability of mouse V2a interneurons. *J. Neurosci.* **2012**, *32*, 13145–13154.
[46] Rossignol, S. Locomotion and its recovery after spinal injury. *Curr. Opin. Neurobiol.* **2000**, *10*, 708–716.
[47] Reichardt, L. F. Neurotrophin-regulated signalling pathways. *Philos. Trans. R. Soc. Lond. B: Biol. Sci.* **2006**, *361*, 1545–1564.
[48] Zhang, R.; Liu, Y.; Yan, K.; Chen, L.; Chen, X. R.; Li, P.; Chen, F. F.; Jiang, X. D. Anti-inflammatory and immunomodulatory mechanisms of mesenchymal stem cell transplantation in experimental traumatic brain injury. *J. Neuroinflamm.* **2013**, *10*, 871.
[49] Bartel, D. P. MicroRNAs: Genomics, biogenesis, mechanism, and function. *Cell* **2004**, *116*, 281–297.
[50] Ahuja, C. S.; Wilson, J. R.; Nori, S.; Kotter, M. R. N.; Druschel, C.; Curt, A.; Fehlings, M. G. Traumatic spinal cord injury. *Nat. Rev. Dis. Primers* **2017**, *3*, 17018.
[51] Sun, Y. Q.; Zhang, Y. L.; Li, X.; Deng, M. X.; Gao, W. X.; Yao, Y.; Chiu, S. M.; Liang, X. T.; Gao, F.; Chan, C. W. et al. Insensitivity of human iPS cells-derived mesenchymal stem cells to interferon-γ-induced HLA expression potentiates repair efficiency of hind limb ischemia in immune humanized NOD scid gamma mice. *Stem Cells* **2015**, *33*, 3452–3467.

[52] Nie, X. Y.; Yuan, T. Y.; Yu, T.; Yun, Z. H.; Yu, T.; Liu, Q. Y. Non-stem cell-derived exosomes: A novel therapeutics for neurotrauma. *J. Nanobiotechnol.* **2024**, *22*, 108.

[53] Pan, W. H.; Banks, W. A.; Kastin, A. J. Permeability of the blood-brain barrier to neurotrophins. *Brain Res.* **1998**, *788*, 87–94.

[54] Han, Q.; Ordaz, J. D.; Liu, N. K.; Richardson, Z.; Wu, W.; Xia, Y. Z.; Qu, W. R.; Wang, Y.; Dai, H. Q.; Zhang, Y. P. et al. Descending motor circuitry required for NT-3 mediated locomotor recovery after spinal cord injury in mice. *Nat. Commun.* **2019**, *10*, 5815.

[55] Yang, Z. Y.; Zhang, A. F.; Duan, H. M.; Zhang, S.; Hao, P.; Ye, K. Q.; Sun, Y. E.; Li, X. G. NT3-chitosan elicits robust endogenous neurogenesis to enable functional recovery after spinal cord injury. *Proc. Natl. Acad. Sci. USA* **2015**, *112*, 13354–13359.

[56] Feng, F.; Song, X. Y.; Tan, Z.; Tu, Y. J.; Xiao, L. Y.; Xie, P. F.; Ma, Y. H.; Sun, X. M.; Ma, J. W.; Rong, L. M. et al. Cooperative assembly of a designer peptide and silk fibroin into hybrid nanofiber gels for neural regeneration after spinal cord injury. *Sci. Adv.* **2023**, *9*, eadg0234.

[57] Dhuria, S. V.; Hanson, L. R.; Frey, W. H. Intranasal delivery to the central nervous system: Mechanisms and experimental considerations. *J. Pharm. Sci.* **2010**, *99*, 1654–1673.

[58] Wiklander, O. P. B.; Nordin, J. Z.; O'Loughlin, A.; Gustafsson, Y.; Corso, G.; Mäger, I.; Vader, P.; Lee, Y.; Sork, H.; Seow, Y. et al. Extracellular vesicle *in vivo* biodistribution is determined by cell source, route of administration and targeting. *J. Extracell. Vesicles* **2015**, *4*, 26316.

[59] Huang, Z. H.; Li, J.; Wo, J.; Li, C. L.; Wu, Z. C.; Deng, X. H.; Liang, Y. Y.; Li, F. X.; Chen, B. L.; Jia, B. et al. Intranasal delivery of brain-derived neurotrophic factor (BDNF)-loaded small extracellular vesicles for treating acute spinal cord injury in rats and monkeys. *J. Extracell. Vesicles* **2025**, *14*, e70066.

[60] Zhou, J. R.; Li, F. X.; Jia, B.; Wu, Z. C.; Huang, Z. H.; He, M. T.; Weng, H. D.; So, K. F.; Qu, W. R.; Fu, Q. L. et al. Intranasal delivery of small extracellular vesicles reduces the progress of amyotrophic lateral sclerosis and the overactivation of complement-coagulation cascade and NF-κB signaling in *SOD1*^{G93A} mice. *J. Nanobiotechnol.* **2024**, *22*, 503.